

Published in final edited form as:

J Am Chem Soc. 2002 June 26; 124(25): 7459–7471.

The Mn Cluster in the S_0 State of the Oxygen-Evolving Complex of Photosystem II Studied by EXAFS Spectroscopy: Are There Three Di- μ -oxo-bridged Mn_2 Moieties in the Tetranuclear Mn Complex?

John H. Robblee^{†,‡,*,}, Johannes Messinger^{†,§,*}, Roehl M. Cinco^{†,‡}, Karen L. McFarlane^{†,⊥}, Carmen Fernandez^{†,‡,||}, Shelly A. Pizarro^{†,‡,#}, Kenneth Sauer^{†,‡,*}, and Vittal K. Yachandra^{†,*}
Melvin Calvin Laboratory, Physical Biosciences Division, Lawrence Berkeley National Laboratory, Berkeley, California 94720, and Department of Chemistry, University of California, Berkeley, California 94720-5230

[†] Lawrence Berkeley National Laboratory.

[‡] University of California, Berkeley.

Abstract

A key component required for an understanding of the mechanism of the evolution of molecular oxygen by the photosynthetic oxygen-evolving complex (OEC) in photosystem II (PS II) is the knowledge of the structures of the Mn cluster in the OEC in each of its intermediate redox states, or S-states. In this paper, we report the first detailed structural characterization using Mn extended X-ray absorption fine structure (EXAFS) spectroscopy of the Mn cluster of the OEC in the S_0 state, which exists immediately after the release of molecular oxygen. On the basis of the EXAFS spectroscopic results, the most likely interpretation is that one of the di- μ -oxo-bridged Mn–Mn moieties in the OEC has increased in distance from 2.7 Å in the dark-stable S_1 state to 2.85 Å in the S_0 state. Furthermore, curve fitting of the distance heterogeneity present in the EXAFS data from the S_0 state leads to the intriguing possibility that three di- μ -oxo-bridged Mn–Mn moieties may exist in the OEC instead of the two di- μ -oxo-bridged Mn–Mn moieties that are widely used in proposed structural models for the OEC. This possibility is developed using novel structural models for the Mn cluster in the OEC which are consistent with the structural information available from EXAFS and the recent X-ray crystallographic structure of PS II at 3.8 Å resolution.

© 2002 American Chemical Society

* To whom correspondence should be addressed. Robblee@mit.edu (J.H.R.), johannes@struktur.chem.tu-berlin.de (J.M.), KHSauer@lbl.gov (K.S.), VKYachandra@lbl.gov (V.K.Y.).

§ Present address: Max Volmer Laboratorium der TU Berlin, PC 14, Strasse des 17. Juni 135, D-10623 Berlin, Germany.

|| Present address: Faculdade de Medicina - Fundação do ABC, Santo André, SP 09060-650 Brazil.

⊥ Present address: Department of Chemistry, Willamette University, 900 State St., Salem, OR 97301.

Present address: Sandia National Laboratories, Biosystems Research Department, P.O. Box 969, MS 9951, Livermore, CA 94551-0969.

¥ Present address: Department of Chemistry, MIT, 77 Massachusetts Ave., Cambridge, MA 02139.

Supporting Information Available: Additional XAS experimental details, comparison of the deconvolution methods for the S_0 state using *E*- and *k*-space data, consideration of possible radiation damage effects, reproducibility of the S_0 EXAFS spectra, and curve-fitting results from Fourier peaks I + II and II + III (PDF). This material is available free of charge via the Internet at <http://pubs.acs.org>.

Introduction

The biological generation of oxygen by the oxygen-evolving complex (OEC) in photosystem II (PS II) is arguably one of nature's most important reactions. To perform the four-electron oxidation of water to dioxygen, the Mn-containing OEC cycles through five intermediate S-states, S_0 through S_4 , as shown in Figure 1. This proposal by Kok et al.¹ in 1970 has led to intense study to identify the nature of each of the quasi-stable S-states S_0 , S_1 , S_2 , and S_3 to derive insight about the mechanism of water oxidation in the OEC. Because the S_1 state is the dark-stable state,¹ this S-state is relatively easily studied in the form of concentrated, dark-adapted samples. The discovery that the S_2 state could be prepared essentially quantitatively by low-temperature (190 K) illumination² allowed similar studies to be performed on the S_2 state as had been done on the S_1 state. However, the remaining S-states, the S_0 state and the S_3 state, required single-flash saturation techniques. Because this was possible only with dilute samples (c5 mg Chl/mL, prior to the experiments detailed in Messinger et al.³), the experimental horizons for these S-states were not very promising, especially for X-ray spectroscopic experiments. This has severely limited experimental studies; hence, much less is known about the S_0 and S_3 states than is known about the S_1 and S_2 states.

Most of the information about the structure of the OEC has come from electron paramagnetic resonance (EPR) and X-ray spectroscopic studies of the S_1 and S_2 states. One form of X-ray spectroscopy, extended X-ray absorption fine structure (EXAFS) spectroscopy, has provided a wealth of information about the structure of the OEC in the S_1 and S_2 states. This is largely due to the inherent element specificity of X-ray spectroscopy. EXAFS studies^{4–13} have firmly established that the OEC in PS II is comprised of di- μ -oxo-bridged Mn_2 clusters which show Mn–Mn scattering at a distance of 2.7 Å. Furthermore, an additional scatterer has been shown to be present at 3.3 Å from Mn,^{7,8,10–12} which has been interpreted as containing contributions from both Mn–Mn and Mn–Ca interactions at 3.3–3.4 Å.^{14,15} These EXAFS-derived structural building blocks have been prerequisite structural elements in virtually any proposed model.^{16–22} However, the models, some of which are shown in Figure 2, are adversely affected by relative paucity of structural information about the S_0 and S_3 states (vide supra). In addition, uncertainty about whether two or three di- μ -oxo-bridged Mn–Mn moieties exist in the Mn cluster has been reflected in the proposed models. To better understand the structure of the Mn cluster, it is therefore important to determine whether it is comprised of two or three di- μ -oxo-bridged Mn–Mn moieties. This is difficult for the S_1 and S_2 states because an accurate determination of the total number of such interactions (the N value from EXAFS curve fitting) is complicated by the inherent error of $\pm 30\%$ in determining the total N value.²³ However, if the samples contain distance heterogeneity in a certain S-state, then the ratio of N values for these slightly different distances, which can be expected to be significantly more accurate than the total N value, can provide additional information on the question of whether two or three di- μ -oxo-bridged Mn–Mn moieties exist in the OEC.

Early XAS experiments by Guiles et al.²⁴ with the S_0 state used chemical treatments to get around the problem of low concentrations. However, the S_0 state generated in this manner was designated as S_0^* to emphasize that it is generated through chemical treatment and is thus not a native S-state. Although hampered by a low signal-to-noise ratio and the uncertainty about the relationship between the chemically generated S_0^* state and the native S_0 state, those experiments provided the first evidence from XAS that heterogeneity may exist in the 2.7 Å Mn–Mn distances in the S_0 state in the form of a reduced amplitude of Fourier peak II in the S_0^* state relative to that in the S_1 state; this heterogeneity is not seen in the S_1 - or S_2 -state EXAFS spectra (but is seen in the S_3 -state EXAFS spectra²⁵).

A separate study by Riggs-Gelasco et al.¹³ examined reduced S-states of the OEC and observed a decrease in the amplitude of the 2.7 Å Mn–Mn Fourier peak. This was interpreted by Riggs-Gelasco et al. as a reduction in the number of Mn–Mn vectors instead of the appearance of distance heterogeneity.

The native S₀ state prepared using single-flash turnover has not been extensively examined using EXAFS spectroscopy due to the difficulties in collecting EXAFS spectra from single-flash saturable samples, although preliminary reports have appeared.^{26,27} In this paper, the method of preparing samples in the native S₀ state described by Messinger et al.²⁸ has been extended to perform EXAFS spectroscopic experiments on the S₀ state of PS II generated through single-flash turnover. These experiments show that, in the S₀ state, heterogeneity most likely exists in the 2.7 Å Mn–Mn distances, which can be explained through the protonation of a di-μ-oxo-bridged Mn–Mn moiety and/or the presence of Mn(II). The presence of distance heterogeneity in the S₀ state has been exploited in the curve-fitting procedure, whose results are suggestive of the possibility that three di-μ-oxo-bridged Mn–Mn moieties exist in the OEC instead of the two di-μ-oxo-bridged Mn–Mn moieties that are widely used in proposed structural models for the OEC.^{10,15–17,19,22,29–32} Possible topological models for the structure of the OEC in the S₀ and S₁ states that are consistent with the EXAFS data from the current study and also with the recent X-ray crystallographic structure of PS II at 3.8 Å resolution³³ are discussed.

Materials and Methods

PS II membranes were prepared from fresh spinach leaves by a 2 min incubation of the isolated thylakoids with the detergent Triton X-100.^{34,35} The samples were then resuspended to a chlorophyll (Chl) concentration of 6.5 mg Chl/mL in sucrose buffer (pH 6.5, 400 mM sucrose, 50 mM MES, 15 mM NaCl, 5 mM MgCl₂, 5 mM CaCl₂) and stored as aliquots at –80 °C until used. Chl concentrations were calculated as described in Porra et al.³⁶

To prepare samples enriched in the S₀ state, a frequency-doubled Nd:YAG laser system (Spectra-Physics PRO 230–10, 800 mJ/pulse at 532 nm, 9 ns pulse width) was used to illuminate the PS II samples. The laser was operated continuously at 10 Hz, and flashes were selected using an external shutter (model LSTX-Y3, nm Laser Products, Inc.).

Before flash illumination, the PS II membranes were diluted to a concentration of 1 mg Chl/mL in sucrose buffer, and 3 mL of this solution was transferred in darkness into each of 20 tissue culture flasks (Falcon 3014, 50 mL, 25 cm² growth area) that were kept on ice. The Nd:YAG beam was redirected and diffused such that the laser beam could illuminate the entire growth area of the flask from below. Sample illumination under these conditions was proven to be saturating by separate experiments in which the Chl concentration was reduced to 0.5 and 0.25 mg Chl/mL, and no increase in the yield of the S₀ state formed in three-flash samples (referred to as 3F sample hereafter) relative to the experiments described herein was seen (data not shown). Each sample was given one pre-flash and was dark-adapted for 90 min on ice.

After dark-adaptation, PPBQ (phenyl-1,4-benzoquinone; 50 mM in MeOH) was added to each flask to a final concentration of 25 μM, and then each sample was illuminated with three flashes at 1 Hz frequency. Immediately after flashing all samples, FCCP (carbonyl cyanide 4-(trifluoromethoxy) phenylhydrazone; 5 mM in MeOH) was added to each flask to a final concentration of 1 μM. This accelerated the deactivation of the S₂ and S₃ states of PS II to the S₁ state³⁷ and reduced Y_D^{ox}, the stable tyrosine radical of PS II.³⁸ The latter reaction essentially eliminates the main path for the decay of the S₀ state, which is the

oxidation of the S_0 state to the S state by Y_D^{ox} .³⁹ This reaction has a half-life of 30 min at 5 °C.⁴⁰ In addition to FCCP, MeOH was added to a final concentration of 3% v/v, which enabled the detection of the S_0 EPR multiline signal (MLS) in these samples (data not shown).^{28,41,42} The samples were collected and centrifuged at 4 °C for 30 min at 48 000g. The concentrated PS II membranes were then put into Lexan sample holders ($22 \times 3.2 \times 0.8$ mm inner dimensions) and were frozen at 77 K for EPR and X-ray experiments. It took a total of 50 min to complete the protocol from the point of flash-induced S_0 -state formation to freezing the samples at 77 K. Control samples in the S_1 state were prepared in an identical fashion, except that the application of three laser flashes to each tissue culture flask was omitted.

EPR spectra were collected on a Varian E-109 spectrometer with an E-102 microwave bridge and stored using Labview running on a Macintosh G3 computer. Samples were maintained at cryogenic temperature using an Air Products Heli-tran liquid helium cryostat. Spectrometer conditions were as follows: S_2 EPR multiline signal, 3300 ± 1000 G scan range, 6300 gain, 30 mW microwave power, 8 K temperature, 32 G modulation amplitude, 100 kHz modulation frequency, 4 min/scan, 1 scan per sample, 0.25 s time constant, 9.26 GHz microwave frequency. MLS amplitudes were determined from the low-field and high-field peak-to-trough measurements for each designated peak in Figure 3. PS II centers in the S_1 state were advanced to the S_2 state by continuous illumination performed at low temperature using a 600 W lamp and a 5% w/v $CuSO_4$ solution as an IR filter. Samples were placed in a tall test tube which was suspended in a 200 K solid CO_2 /ethanol bath. An unsilvered dewar contained the 200 K bath and enabled the low-temperature illuminations.

EXAFS spectra were recorded on beamline 7-3 at SSRL (Stanford Synchrotron Radiation Laboratory) essentially as described in DeRose et al.¹¹ and Latimer et al.¹⁴ Additional details are provided in the Supporting Information. Two sample regions of 1.4 mm height were used, and eight scans were collected from each separate region. The samples were protected with a shutter from the X-ray beam at all times unless a measurement was in progress. Sixteen scans (eight scans per region, two regions per sample) were averaged per sample for each of six 3F samples and six control samples in the S_1 state.

Data reduction of the EXAFS spectra was performed essentially as described in DeRose et al.¹¹ and Latimer et al.¹⁴ Curve fitting was performed using ab initio-calculated phases and amplitudes from the program FEFF 7.02 from the University of Washington.⁴³⁻⁴⁶ These ab initio phases and amplitudes were used in the EXAFS equation,⁴⁷⁻⁵⁰ shown as eq 1:

$$\chi(k) = S_0^2 \sum_j \frac{N_j}{k R_j^2} f_{eff,j}(\pi, k, R_j) e^{-2\sigma_j^2 k^2} e^{-2R_j/\lambda_j(k)} \sin(2kR_j + \phi_{ij}(k)) \quad (1)$$

S_0^2 is an amplitude reduction factor due to shake-up/shake-off processes at the central atom(s). This factor was set to 0.85 for all fits, on the basis of fits to model compounds.⁵¹ The neighboring atoms to the central atom(s) are then divided into j shells, with all atoms with the same atomic number and distance from the central atom grouped into a single shell. Within each shell, the coordination number N_j denotes the number of neighboring atoms in shell j at a distance of R_j from the central atom. $f_{eff,j}(\pi, k, R_j)$ is the ab initio amplitude function for shell j , and the Debye–Waller term $e^{-2\sigma_j^2 k^2}$ accounts for damping due to static and thermal disorder in absorber–backscatterer distances. A larger Debye–Waller factor σ_j reflects increased disorder, and leads to an exponential damping of the EXAFS oscillations. The mean free path term $e^{-2R_j/\lambda_j(k)}$, which depends on k (the momentum of the photoelectron), reflects losses due to inelastic scattering, where $\lambda_j(k)$ is the electron mean free path.⁵⁰ $\lambda_j(k)$ was calculated by ab initio methods using FEFF 7.02. The oscillations in the EXAFS spectrum are reflected in the sinusoidal term $\sin(2kR_j + \phi_{ij}(k))$, where $\phi_{ij}(k)$ is

the ab initio phase function for shell j . This sinusoidal term shows the direct relation between the frequency of the EXAFS oscillations in k -space and the absorber-backscatterer distance.

Equation 1 was used to fit the experimental Fourier isolates using N , R , and σ^2 as variable parameters. No firm theoretical basis exists to guide the choice of E_0 for Mn K-edges; thus, uncertainty in E_0 translates into uncertainty in k -space values (see eq S1 in the Supporting Information). Therefore, E_0 was also treated as a variable parameter. To reduce the number of free parameters in the fits, the value of E_0 was constrained to be equal for all shells in the fit. This was shown by O'Day et al.⁵² to be a valid constraint when using FEFF phases and amplitudes.

N values are defined as shown in eq 2:

$$N = \frac{\text{total number of Mn-backscatterer vectors}}{\text{number of Mn atoms per OEC}} \quad (2)$$

Hence, coordination numbers are evaluated on a per Mn basis and are dependent on the stoichiometry of Mn atoms in the OEC. It is well established that an active OEC contains four Mn atoms;^{6,53–64} a report of six Mn per PS II⁶⁵ was most likely due to an uncorrected high residual Mn content in inactive centers present in the samples.⁶⁶ On a four Mn/PS II basis, N values for Mn–Mn interactions in the OEC come in multiples of 0.5, because each Mn–Mn interaction contains two Mn–backscatterer interactions. Other Mn–backscatterer interactions come in multiples of 0.25; that is, an N value of 2 in a Mn–O shell is interpreted as two O neighbors to each Mn atom.

The ability of the EXAFS technique to resolve the presence of similar backscatterers at closely separated distances is well known to be dependent on ΔR , the difference in absorber-backscatterer distances (\AA), and Δk , the width of the k -space EXAFS data set (\AA^{-1}). When EXAFS oscillations from two backscatterers at closely separated distances are superimposed, the addition of the sinusoidal terms from eq 1 ($\sin[2kR_1]$ and $\sin[2kR_2]$, if the phase shifts are identical) generates a local amplitude minimum in the k -space spectrum from the addition of two sine waves with different frequencies; this is commonly known as a beat. The magnitude of $R_1 - R_2$ determines at what value of k the beat will appear. This is shown by the trigonometric identity in eq 3:

$$\sin a + \sin b = 2 \cos\left(\frac{a-b}{2}\right) \sin\left(\frac{a+b}{2}\right) \quad (3)$$

Equation 4 shows the application of eq 3 to the current problem:

$$\sin 2kR_1 + \sin 2kR_2 = 2 \cos(k[R_1 - R_2]) \sin(k[R_1 + R_2]) \quad (4)$$

The beat in the k -space spectrum arises from the $\cos(k[R_1 - R_2])$ term in eq 4. When the cosine function equals zero, the first beat will appear. This occurs when eq 5 is true:

$$k[R_1 - R_2] = \frac{\pi}{2} \quad (5)$$

Thus, the minimum ΔR necessary to see a beat in the k -space spectrum is most accurately depicted by eq 6, assuming that the k -space window is wide enough to see the beat.^{67–71}

$$\Delta R = \frac{\pi}{2k_{\max}} \quad (6)$$

It should be noted that other formulas, such as $\Delta R \Delta k \approx 1$ and $\Delta R \Delta k = (\pi/2)$, are often seen in the EXAFS literature^{50,72–76} and do not predict the correct resolution limit.

Fit quality was evaluated using two different fit parameters, Φ and ϵ^2 . Φ is described in eq 7:

$$\Phi = \sum_1^{N_T} \left(\frac{1}{s_i} \right)^2 \left[\chi^{\text{expt}}(k_i) - \chi^{\text{calc}}(k_i) \right]^2 \quad (7)$$

where N_T is the total number of data points collected, $\chi^{\text{expt}}(k_i)$ is the experimental EXAFS amplitude at point i , and $\chi^{\text{calc}}(k_i)$ is the theoretical EXAFS amplitude at point i . The normalization factor s_i is given by eq 8:

$$\frac{1}{s_i} = \frac{k_i^3}{\sum_j^N k_j^3 |\chi^{\text{expt}}(k_j)|} \quad (8)$$

The ϵ^2 error takes into account the number of variable parameters p in the fit and the number of independent data points N_{ind} , as shown in eq 9:^{77,78}

$$\epsilon^2 = \left[\frac{N_{\text{ind}}}{N_{\text{ind}} - p} \right] N_T^{-1} \Phi \quad (9)$$

N_T is the total number of data points collected, and the number of independent data points N_{ind} is estimated from the Nyquist sampling theorem, as shown in eq 10:

$$N_{\text{ind}} = \frac{2\Delta k \Delta R}{\pi} \quad (10)$$

Δk is the k -range of the data (3.5–11.5 Å⁻¹), and ΔR is the width of the Fourier-filtered peak in Å. ϵ^2 provides a gauge of whether the addition of another shell to the fit is justified. If, upon addition of a second shell, ϵ^2 becomes negative, then there are not enough free parameters available to statistically justify the inclusion of the additional shell. An acceptable model, of which there may be more than one, is any one for which ϵ^2 differs by a factor of less than two.

Results

EPR

It is critical that an independent determination of the S-state distribution of the three-flash (3F) samples is performed using EPR spectroscopy; this information is required for the deconvolution of the 3F EXAFS spectra to obtain the spectra of the “pure” S_0 state. Because FCCP was added to the samples immediately after the flashes, any centers that remain in the S_2 or S_3 states after the flash treatment are rapidly deactivated to the S_1 state,³⁷ as explained in the Materials and Methods section. Therefore, the calculated S-state distribution will contain PS II centers in only the S_0 and S_1 states. In separate experiments, it was discovered that increasing the FCCP concentration 10-fold (to 10 μM) caused an ~25% conversion of the S_1 state in the dark to the S_0 state and possibly the S_{-1} state (data not shown). To confirm that the FCCP concentration used in this study (1 μM) was not of sufficient

concentration to cause reduction of the S_1 state, the S_2 -state EPR multiline signal was measured from parallel S_1 -state samples with and without FCCP that had been continuously illuminated at 200 K. The fact that identical normalized S_2 -state EPR multiline signal amplitudes were obtained from both types of samples argues against reduction of the S_1 state by FCCP under the conditions used in this study.

During the preparation of the XAS samples, eight identical 3F samples and eight identical S_1 -state samples were prepared. From these 16 samples, two S_1 -state samples and two 3F samples were set aside for EPR characterization. Because the samples that were set aside for EPR characterization and the respective samples used in the XAS experiments are all aliquots from the same PS II solution, the S-state distribution that was determined for the samples characterized by EPR can also be used to deconvolute the EXAFS spectra for the XAS samples.

The S_2 -state multiline EPR signal generated by continuous illumination (CI) at 190 K of the 3F and S_1 -state samples is shown in Figure 3. At 190 K, all S-state transitions except for the $S_1 \rightarrow S_2$ transition are blocked.⁷⁹ This means that, in the 3F sample, the S_0 state cannot advance to the S_1 or S_2 states during this illumination procedure; thus the 3F CI samples will have a smaller normalized S_2 -state multiline EPR signal than will the S_1 -state CI samples. In addition, because the spectra shown in Figure 3 are difference spectra (after CI – before CI), the presence of the S_0 -state multiline EPR signal,^{28,41,42} which was visible in the 3F samples before CI (data not shown), will not affect the quantitations of the S_2 -state multiline EPR signal. To correct for differences in sample volume, the measured S_2 -state multiline EPR signals for each sample were normalized by the magnitude of their respective rhombic Fe^{2+} signal.

The results of the EPR characterization study are shown in Table 1. The ratio of the induced S_2 -state multiline EPR signal in the 3F sample relative to that induced in the control S_1 -state sample (50%) corresponds to the percentage of centers originally in the S_1 state in the 3F sample. Therefore, the S-state distribution assigned to the samples in the current study is 50% S_0 , 50% S_1 . This S-state distribution will be used in subsequent deconvolutions of the EXAFS spectra of 3F samples. To examine the effects of possible deconvolution error, two additional S-state distributions were also considered during the fitting procedure: 40% S_0 , 60% S_1 and 60% S_0 , 40% S_1 .

By using samples with a final Chl concentration of 9.5 mg Chl/mL and freezing the samples immediately after the flash protocol, a greater S_0 -state percentage (65% according to Table 2 from Messinger et al.³) was obtained in the 3F samples in the experiments described in Messinger et al.³ than the S_0 -state percentage reported in the current study. The smaller S_0 -state percentage is most likely due to the oxidation of some of the centers in the S_0 state during the 30 min centrifugation and subsequent sample handling by Y_D^{ox} residues which have not yet been reduced by FCCP. However, having a lower percentage of centers in the S_0 state for the S_0 -state EXAFS experiments is necessary to ensure that the only other S-state is the S_1 state (which is well characterized) and to obtain highly concentrated PS II samples for EXAFS studies.

EXAFS. EXAFS Spectra (k^3 -weighted) and Fourier Transforms

The average Mn K-edge EXAFS spectra from six 3F samples and six samples in the S_1 state were used to deconvolute the 3F spectrum into the EXAFS spectrum of the pure S_0 state, using the S-state distribution determined from Figure 3 (shown in Table 1 as 50% S_0 , 50% S_1). These average k^3 -weighted spectra for the S_1 state and the deconvoluted S_0 state are shown in Figure 4. The deconvolution was performed using normalized E -space spectra before conversion into k -space. When the deconvolution was performed after both the 3F

spectrum and the S_1 state were converted into k -space, the results were virtually identical (see Figures S1 and S2 in the Supporting Information). Furthermore, there is almost no difference in the k^3 -weighted spectra if the first two EXAFS scans from each region of the sample are compared to the last two EXAFS scans from each region of the sample (see Figure S3 in the Supporting Information). In addition, there was no discernible difference in the fits to the EXAFS data for the two k^3 -weighted spectra (data not shown). Therefore, the effects of photoreduction are assumed to be negligible.

The most noticeable change between the S_0 -state and S_1 -state spectra is that the resolution of EXAFS oscillations in the S_1 state between $k = 8.5$ and 11 \AA^{-1} is decreased in the S_0 state and the frequency of the oscillations is different between the two S-states. This can be explained by an increase in distance heterogeneity in the S_0 state relative to the S_1 state, which leads to destructive interference at higher k values of EXAFS oscillations of slightly different frequencies. This phenomenon has also been seen in other S-states that have heterogeneity in the Mn–Mn distances, such as the S_0^* state,²⁴ the S_2 ($g = 4.1$) state,⁸⁰ the NH_3 -treated S_2 state,⁸¹ the F^- -treated S_2 state,⁸² and the S_3 state.^{25,83} Each of the six 3F samples that were used to generate the average spectrum shown in Figure 4 was deconvoluted separately using the average S_1 -state EXAFS spectrum to generate six independent S_0 -state EXAFS spectra; the results are shown in Figure S4 in the Supporting Information. This shows that the loss of resolution of the EXAFS oscillations that is seen in the average spectrum is also seen in the spectra from the six individual samples.

By performing a Fourier transform on the k^3 -weighted spectra, a graphical representation of the environment surrounding the Mn atoms in PS II is obtained as a radial distribution function.⁸⁴ Figure 5 shows the Fourier transforms from the S_0 -state and S_1 -state k^3 -weighted spectra shown in Figure 4. Three prominent peaks, labeled as peaks I, II, and III in Figure 5, exist in the Fourier transforms. Peak I corresponds to first-shell Mn–O interactions arising from μ -oxo-bridging and terminal ligands. Peak II arises from Mn–Mn backscattering in di- μ -oxo-bridged Mn_2 moieties. Peak III has been proposed to contain contributions from both mono- μ -oxo-bridged Mn–Mn and mono- μ -oxo-bridged Mn–Ca moieties, although other bridging motifs, such as μ -1,1-carboxylato and μ -hydroxo, are possible.

Although peak III is relatively invariant between the S_0 and S_1 states, peaks I and II show significant differences between the S_0 and S_1 states. Peak I is at a longer apparent distance and has a slightly lower peak amplitude in the S_0 state relative to the S_1 state. This implies an increase in distance and/or distance heterogeneity in the Mn–O distances in the S_0 state relative to the S_1 state. In the S_0 state, peak II is approximately 30% lower in amplitude than in the S_1 state. This consequence of the aforementioned loss in resolution of EXAFS oscillations in the k -space spectrum of the S_0 state was also seen in the previously mentioned studies of other S-states that have heterogeneity in the Mn–Mn distances.^{24,25,80–83} This provides compelling evidence that structural changes occur during the $S_0 \rightarrow S_1$ transition that reduce the heterogeneity of the 2.7 \AA Mn–Mn distances.

Curve Fitting of EXAFS Spectra

The Fourier transforms shown in Figure 5 provide the basis for drawing qualitative conclusions about structural changes during the $S_0 \rightarrow S_1$ transition. Reliable quantitative results can be obtained by fitting the experimental data using the EXAFS equation (eq 1), as described in the Materials and Methods section. The Fourier isolates of peaks I, II, and III are shown in Figure 6, Figure 7, and Figure 8, respectively; these isolates show the k^3 -weighted contributions to each Fourier peak. The increase in the apparent distance of peak I in the Fourier transforms of the S_0 state relative to the S_1 state is evident in the increase in frequency of the EXAFS oscillations in the S_0 -state Fourier isolate relative to that of the S_1 -state, as shown in Figure 6. For peak II, the amplitude of the S_0 -state Fourier isolate in

Figure 7 is significantly smaller than that of the corresponding S_1 -state Fourier isolate. Because the amplitude envelope for the S_0 -state Fourier isolate is significantly different from that of the S_1 state (maximum for the S_0 state is at $\sim 8 \text{ \AA}^{-1}$ and S_1 state is at $\sim 9 \text{ \AA}^{-1}$; see Figure 7), it is unlikely that the decrease in peak II amplitude can be explained by a decrease in the number of Mn–Mn interactions in the S_0 state relative to the S_1 state, which should not change the amplitude envelope. A more likely origin, which was stated earlier, is the presence of distance heterogeneity in the Mn–Mn distances in the S_0 state. If the ΔR value is smaller than the theoretical resolution limit of 0.14 \AA (see Materials and Methods for details), the observed damping of the amplitude function would occur. The fit results shown in the Curve Fitting of EXAFS Spectra section show that the calculated distance separation from the fits is, in fact, close to the theoretical resolution limit (vide infra). To see a beat in the Fourier isolates at the proposed distance separation in the S_0 state, the EXAFS spectrum would have to be collected to higher k values. Unfortunately, the Fe K-edge occurs at a k value of approximately 12 \AA^{-1} . Because there are two to three Fe atoms per OEC (one or two copies of cytochrome b_{559} and one non-heme Fe^{2+})⁸⁵ and extra Fe can be present in the preparation depending on isolation conditions,⁶⁰ this makes it very difficult to collect data at higher k values.

The Fourier isolates from peak II from each individual S_0 -state data set are shown in Figure S5 in the Supporting Information. These Fourier isolates show that the trends seen in the Fourier isolate generated from the Fourier transform of the average S_0 -state spectrum are also seen in the Fourier isolates generated from each individual sample.

Fourier Peak I

Fits to peak I are known to be dominated by the 1.8 \AA bridging Mn–O distances,¹¹ although more terminal Mn–O distances exist than bridging Mn–O distances. This is due to the two types of distances having different disorder parameters.¹¹ Thus, using one Mn–O shell, fits #1–8 in Table 2 show that the S_0 state is best fit by a 1.86 \AA Mn–O distance. This is a longer distance than the corresponding fit to the S_1 -state spectrum (fit #9 in Table 2), which is 1.84 \AA .

To account for the two different types of Mn–O distances (bridging and terminal), two-shell fits to peak I were attempted, although some previous studies have been unable to detect the presence of the Mn–O (terminal) shell.⁵¹ Fits #10 and #11 in Table 2 show one fit minimum for a two-shell fit to peak I for the S_0 state and one for the S_1 state. A significant improvement in fit error Φ is seen for the two-shell fit. However, these two-shell fit minima are quite shallow; essentially identical fit error values were obtained if the N and Debye–Waller values for the Mn–O (terminal) shell were both much smaller (0.5 – 1.0 and $\sim 0.002 \text{ \AA}^2$, respectively), or were both at an intermediate value. Irrespective of the N and σ^2 values, however, the R values for the Mn–O (terminal) distances in the S_0 and S_1 states were much more precise. The Mn–O (terminal) shell for the S_0 state required a long 2.2 – 2.3 \AA distance for an acceptable fit, as compared to the 2.0 – 2.1 \AA distance that was required for the S_1 state. A logical extension of this fit, if Mn(II) is present in the S_0 state, is to attempt a three-shell fit that separates the Mn–O (bridging) distances, the Mn(II) Mn–O (terminal) distances, and the Mn–O (terminal) distances from the other three Mn atoms into separate shells. However, this resulted in an underdetermined fit as calculated by eq 9 because of the limited width of the Fourier peak (see eq 10).

A reasonable conclusion from the fits to peak I is that there is an increase in the Mn–O distances in the S_0 state relative to the S_1 state, which is also seen in the Fourier isolates shown in Figure 6 and the Fourier transforms shown in Figure 5. This can be accounted for by the 0.02 \AA increase in the average Mn–O (bridging) distance in the S_0 state relative to the

S_1 state. This conclusion is consistent with, but cannot prove, the presence of a Mn(II) atom in the S_0 state.

Fourier Peak II

Relative to peaks I and III, fits to peak II are well known to have deep fit minima and thus produce the most reliable information about neighbors to Mn in the OEC.¹¹ The qualitative analysis of the S_0 - and S_1 -state EXAFS data (see above) indicates that a more pronounced Mn–Mn distance heterogeneity exists in S_0 state than in the S_1 state. In principle, this heterogeneity can be caused by either increased disorder of one Mn–Mn distance or the presence of two (or more) distinct Mn–Mn distances of slightly different length. We tested these two possibilities by comparing one-shell fits with two-shell fits.

Fits #1–9 in Table 3 show the results from fitting one Mn–Mn shell to peak II in both the S_0 and the S_1 states. A high disorder of one Mn–Mn distance is expected to reveal itself by high Debye–Waller factor in the one-shell fits. Table 3 shows indeed that in fits of the S_0 -state data, the Debye–Waller factor is about 2–2.5 times as large as for the S_1 -state data. No differences in the Mn–Mn distance are observed under these fit conditions between the S_0 and S_1 states.

Fits #10–17 in Table 3 show improvements in the fits for the S_0 state if peak II is treated as two separate Mn–Mn distances. Attempts to fit the second shell as a Mn–C shell and the first shell as a Mn–Mn shell produced significantly (2–3-fold) higher fit error values than the one-shell Mn–Mn fits (data not shown); thus, this scenario is considered unlikely. With two separate Mn–Mn distances, the fit error Φ decreased by 40% for the two-shell fit in the S_0 state relative to the one-shell fit, indicating that splitting the Mn–Mn distances is a valid approach. However, the improvement in Φ for the S_1 state is only 19% for the same approach.

Furthermore, the fit results from the two-shell fit (fit #18 from Table 3), which show distance heterogeneity in the Mn–Mn distances in the S_1 state for this fit, are inconsistent with the low (0.002 \AA^2) Debye–Waller factor for the one-shell fit in the S_1 state. Curve-fitting results from Mn model compound EXAFS data⁵¹ show that Mn–Mn shells with no distance heterogeneity exhibit Debye–Waller factor values of 0.002 \AA^2 . Thus, it may not be meaningful to apply a two-shell fit to peak II in the S_1 state, and Mn–Mn distance heterogeneity in the S_1 state is marginal at best.

Table 4 shows the results from two-shell fits to peak II. The results from Table 4 expand on the possible inequality between N_1 and N_2 by using the constraint that there must be an integral number of Mn–Mn interactions. To test the case of constant disorder of two separate Mn–Mn distances, we fixed the Debye–Waller factor to 0.002 \AA^2 , the value observed for the S_1 -state data and in model compound studies.⁵¹ We furthermore varied only N_1 and fixed the $N_1:N_2$ ratio to chemically reasonable values of 1:1 (fits #1–9) or 2:1 (fits #10–18) (Table 4). This corresponds to the scenarios of two Mn–Mn interactions ($N_1:N_2 = 1:1$) and three Mn–Mn interactions ($N_1:N_2 = 2:1$), respectively. E_0 was restrained to be identical for all subshells. This allows a direct comparison of Φ (and ϵ^2 values) between these different fits. For the S_1 state, the fit quality was essentially identical in all cases, so there is no compelling reason to invoke a distance heterogeneity. This is true especially also in light of the small Debye–Waller factor of the one-shell fit (fit 9, Table 3). It is important to note that, regardless of which $N_1:N_2$ ratio was applied, there was no improvement in Φ or ϵ^2 for the S_1 -state two-shell fits relative to the single-shell fits, indicating that, if three Mn–Mn 2.7 \AA distances exist in the S_1 state, there is no resolvable distance heterogeneity in these experiments. An almost identical fit quality is also observed for the one-shell and the two-shell fits of the S_0 state, when the $N_1:N_2$ ratio was fixed to 1:1. However, an improvement of

the fit quality by about 30% is observed for the S_0 state, if the $N_1:N_2$ ratio was fixed to 2:1 (fits #10–17 from Table 4). Furthermore, the N_1 and N_2 values for all of the S_0 -state fits are close to 1 and 0.5, respectively. The Mn–Mn distances for these S_0 -state fits are quite similar to those from Table 3, with $R_1 = 2.72$ Å and $R_2 = 2.85$ Å ($\Delta R = 0.13$ Å).

The above analysis favors the case where two distinct Mn–Mn distances of 2.72 and 2.85 Å contribute to peak II of the S_0 -state samples. This observation is in agreement with earlier data of other samples with a decreased peak II amplitude: the NH_3 -treated S_2 -state⁸¹ and the S_3 -state⁸³ dichroism studies on oriented PS II membranes have confirmed the presence of distance heterogeneity and two separate Mn–Mn distances in peak II, because significant differences are seen in the dichroism properties of the different Mn–Mn vectors.

The findings that a $N_1:N_2$ ratio of 2:1 gives clearly a better fit than a ratio of 1:1 and that the total $N = N_1 + N_2$ is about 1.5 have the intriguing implication that three and not two di- μ -oxo-bridged type Mn–Mn distances may exist in the OEC, and that one of them is longer in the S_0 state relative to those in the S_1 state.

The two-shell fit to peak II can also be displayed graphically as a contour plot, as shown for the S_0 state in Figure 9. In this plot, the N_1 and N_2 values corresponding to the Mn–Mn distances from each shell are fixed at the designated values for each fit. The S_0 -state contour plot in Figure 9 shows that a well-defined fit minimum exists at $N_1 = 1.05$ and $N_2 = 0.46$, which corresponds to 2.1 Mn–Mn interactions at ~ 2.7 Å and 0.92 Mn–Mn interactions at ~ 2.85 Å. As expected, this is the same fit minimum that exists in fit #17 from Table 3. Thus, Figure 9 provides strong visual confirmation that the two-shell fits to peak II from the S_0 state asymmetrically distribute N_1 and N_2 values, and therefore the 2.7 and 2.85 Å Mn–Mn distances, in a 2:1 ratio. Although a clear minimum for Φ is observed for the case of two 2.7 Å and one 2.85 Å Mn–Mn vectors, the case of one 2.7 Å and one 2.85 Å Mn–Mn vector, or a site inhomogeneity are less likely, but may not be ruled out by our current data.

Because the proposed distance heterogeneity in the S_0 state (0.13–0.14 Å) is so close to the theoretical resolution limit of 0.14 Å, it is not possible to unequivocally prove that there are two different Mn–Mn distances present in the S_0 state. This resolution limit is defined as the ability to see a k^3 -weighted beat in the peak II Fourier isolate, and can be improved if data can be collected to higher k values (see Materials and Methods for a discussion of the calculation of theoretical resolution limits). Thus, it is possible to explain the EXAFS data from the S_0 state in terms of an overall increase in site inhomogeneity for the 2.7 Å distances. This is a different disorder scenario from the presence of two different Mn–Mn distances, which would be expected to have very little site inhomogeneity.

Fourier Peak III

Curve-fitting results for peak III are shown in Table 5. The fit results for the individual S_0 -state samples were essentially identical to those shown in Table 5 for the S_0 grand add fit (data not shown). Although the fit minima are much more shallow than those for fits to peak II, it is still possible to address some relevant questions about peak III, specifically the chemical nature of the backscatterers that contribute to this peak. A comparison of fits #1 and #2, as well as fits #4 and #5, shows that the fit results are slightly better if peak III is fit with a Mn–Mn rather than a Mn–Ca distance. Fits #3 and #6 show that the fit error parameters Φ and ε^2 drop by a sizable amount, approximately 50%, if an additional Mn–Ca interaction is added to the mono- μ -oxo Mn–Mn interaction. Attempts to fit peak III with a combination of a Mn–Mn shell and a Mn–C shell or a combination of a Mn–Ca shell and a Mn–C shell resulted in fit errors that were 2–3-fold higher than those for a combination of a Mn–Mn shell and a Mn–Ca shell (data not shown). A similar increase in error was observed if the N value for fit #1 or fit #4 in Table 5 was fixed to 1.0 to assess the possibility of two or

more 3.3 Å Mn–Mn interactions or if peak III was fit with only a Mn–C shell (data not shown). In addition, attempts to fit peak III with one Mn–Mn shell ($N = 0.5$) and two Mn–Ca shells ($N = 0.5$) resulted in fit errors that were 20–50% higher than those shown for fits #3 and #6 in Table 5. As shown in the Fourier transforms from Figure 5, peak III is essentially invariant between the S_0 state and the S_1 state. Thus, it is not surprising that the fits are quite similar between the S_0 and the S_1 states. The Fourier isolate from Figure 8 shows a very small frequency shift between the S_0 and the S_1 states which is manifested in slightly smaller (0.02–0.03 Å) distances in the S_0 state relative to the S_1 state. However, these changes may be too small to be significant.

Controls

All of the previous fits to peaks I, II, and III were also applied to the average EXAFS spectrum from the 3F samples (50% S_0 , 50% S_1) to examine the consequences of the subtraction procedure. Because of the high signal-to-noise ratio achieved in this experiment, it is unlikely that the fit results presented in Tables 2–5 are the result of noise introduced into the data during the subtraction procedure. The fits to the EXAFS spectra from the 3F samples confirmed this, because the fit results were halfway between those reported above for the S_0 state and those reported above for the S_1 state (data not shown). Furthermore, the same fitting approach was applied to S_0 -state spectra obtained from 3F-sample spectra using the alternative deconvolutions mentioned earlier (40% S_0 , 60% S_1 and 60% S_0 , 40% S_1), and almost identical results were found between these fits and those shown in Tables 2–5 (data not shown). This makes it highly unlikely that the observed differences between the S_0 -state and S_1 -state EXAFS spectra, as well as the 2:1 ratio for $N_1:N_2$, arise from errors in deconvolution.

As mentioned in the Materials and Methods section, the possibility was examined that the Fourier isolation technique is generating artifacts in the data, although most of the Fourier peaks in Figure 5 are well separated, which minimizes any distortion artifacts from the isolation procedure. This possibility was addressed by isolating the Fourier peaks as pairs (peaks I + II and peaks II + III) and comparing the obtained curve-fitting results to those obtained when the peaks were isolated individually. As shown in Tables S1 and S2 in the Supporting Information, no major changes in the fit results are obtained by fitting the Fourier peaks as pairs relative to the fits to the individual Fourier peaks; thus, it is rather unlikely that the fit results presented in Tables 2–5 are affected by Fourier isolation artifacts.

Discussion

Mn–Mn Distance Heterogeneity in the OEC

As mentioned in the Introduction, EXAFS experiments have shown that a major structural motif in the OEC is the di- μ -oxo-bridged binuclear Mn_2 unit.^{4–12} The additional presence of mono- μ -oxo Mn–Mn and Mn–Ca motifs at a longer distance has also been shown, although the bridging motif could also be mono- μ -carboxylato or mono- μ -hydroxo.^{7,8,10–12,14} EXAFS studies of the S_1 and S_2 states revealed that all of the di- μ -oxo-bridged Mn–Mn moieties have essentially the same Mn–Mn distance of ~2.7 Å. This distance is consistent with those found in numerous studies of di- μ -oxo-bridged $Mn_2(III,IV)$ and $Mn_2(IV,-IV)$ complexes.^{4,86,87} This provides strong evidence that the 2.7 Å distance detectable in the EXAFS spectra of the S_1 and S_2 states originates from di- μ -oxo-bridged $Mn_2(III,IV)$ and/or $Mn_2(IV,IV)$ moieties.

However, other states of the OEC, including those generated by treatments with oxygen-evolution inhibitors, show that many of these states contain Mn–Mn distance heterogeneity which affects the amplitude and, in some cases, the position of peak II in the Fourier

transforms. EXAFS studies of the S_2 ($g = 4.1$) state,⁸⁰ the F^- -treated S_2 state,⁸² and the NH_3 -treated S_2 state⁸¹ all show that one of the Mn–Mn distances has increased to 2.8–2.85 Å. In the native S_3 state, EXAFS detects the presence of at least two Mn–Mn distances which have increased in length to 2.85 and 3.0 Å relative to the S_1 -state distances of 2.7 Å.^{25,83}

The results from the current study represent the first EXAFS characterization of the native S_0 state. A previous study by Guiles et al.²⁴ characterized a chemically reduced S-state called the S_0^* state, and provided evidence for Mn–Mn distance heterogeneity in that S-state in the form of a lower peak II amplitude in the S_0^* state. The results from the current study show that the S_0 state has a noticeable reduction in the amplitude of peak II in the Fourier transform relative to the S_1 state, as seen in Figure 5. This can be explained by the existence of Mn–Mn distance heterogeneity in the S_0 state in the form of Mn–Mn distances at ~2.7 and ~2.85 Å. These results provide the first evidence that structural changes occur during the $S_0 \rightarrow S_1$ transition in the OEC, which can be rationalized by a combination of two effects: μ -oxo bridge protonation and/or the presence of Mn(II) in the S_0 state.

The plausibility of μ -oxo bridge protonation in the S_0 state comes from an EXAFS spectroscopic study by Baldwin et al.⁸⁸ of a series of $Mn_2(IV,IV)$ di- μ -oxo-bridged complexes in which the μ -oxo bridges were successively protonated. The results from this study showed that the Mn–Mn distance increases from 2.7 to 2.8 to 2.9 Å with 0, 1, or 2 μ -oxo bridge protonations, respectively. This can be explained by the fact that protonation of a μ -oxo bridge lowers the Mn–O bond order, which causes an increase in the Mn–Mn distance. Protonation of a μ -oxo bridge could occur as a consequence of the lower Mn average oxidation state in S_0 and/or due to rebinding of substrate water to the Mn cluster in the $S_4 \rightarrow S_0$ transition.

Another effect that could increase the Mn–Mn distance is the presence of Mn(II). It is well known that the Mn–ligand distances are longer for Mn(II) complexes than they are for Mn-(III) and Mn(IV) complexes,^{89–91} and the XANES and $K\beta$ spectroscopic data from Messinger et al.³ are consistent with the presence of Mn(II) in the S_0 state. However, no Mn model complexes have been reported which contain a di- μ -oxo-bridged Mn(II) atom. The closest analogues which have been structurally characterized are $Mn_2(II,II)$ and $Mn_2(II,III)$ di- μ -phenoxyl-bridged complexes which have Mn–Mn distances of 3.2–3.4 Å.^{92–96} In addition, a di- μ -hydroxo-bridged $Mn_2(II,II)$ complex with a Mn–Mn distance of 3.31 Å has been characterized.⁹⁷ The long Mn–Mn distance in these complexes is most likely due to a combination of the nature of the bridging ligands and the oxidation states of the Mn ions; a di- μ -oxo-bridged moiety that incorporates Mn(II) along with Mn(III) or Mn(IV) would be expected to have a shorter Mn–Mn distance than is seen in the above-mentioned complexes due to the presence of the μ -oxo bridges.

It is also possible that both of these features, the presence of Mn(II) and μ -oxo bridge protonation, occur in the S_0 state.

Are There Three Di- μ -oxo Bridges Present in the OEC?

Analysis of the results presented in this paper shows that it is possible that three, not two, di- μ -oxo Mn–Mn moieties are present in the OEC. This conclusion is a result of the finding that the fits to Fourier peak II in the S_0 state shown in Table 4 do not favor an equal distribution of the coordination numbers N_1 and N_2 between the 2.7 and the 2.85 Å shells; an equal distribution would be consistent with the presence of two di- μ -oxo Mn–Mn moieties. Instead, clearly better results are seen when the distribution of N values is 2:1 with $N_{tot} \sim 1.5$. Although EXAFS spectroscopic results have been consistent with two to three di- μ -oxo-

bridged Mn–Mn moieties, proposed models^{17,19,30–32} (including our own^{10,15,16,22,29}) have emphasized two di- μ -oxo-bridged Mn–Mn moieties.

Because the possibility that three di- μ -oxo Mn–Mn moieties exist in the OEC has not been seriously considered until now,⁷⁴ it is productive to reexamine the data already in the literature under the premise of three di- μ -oxo Mn–Mn moieties. This is most convincingly done for S-states in which Mn–Mn distance heterogeneity exists, because the $N_1:N_2$ ratio for these S-states can be examined. As mentioned earlier, we expect this to be more reliable than examining the total N value from EXAFS curve-fitting of the S_1 and S_2 states, which can be different from the actual N value by up to 30%.²³ The S-states of interest include the S_0^* state,²⁴ the S_2 ($g = 4.1$) state,⁸⁰ the NH_3 -treated S_2 state,⁸¹ the F^- -treated S_2 state,⁸² and the S_3 state.^{25,83}

The results of this reexamination are shown in Table 6, which show that none of the S-states which exhibit distance heterogeneity is best fit by an equal N value for both Mn–Mn shells; the fit results from these S-states are, in fact, more consistent with a 2:1 $N_1:N_2$ ratio (where N_1 corresponds to the shorter distance), as seen in the data from the current study.

Mechanistic and Structural Consequences

The data from the current study and a reinterpretation of data already in the literature are consistent with two or three Mn–Mn di- μ -oxo bridges in the OEC, favoring three based on the $N_1:N_2$ ratios in samples with heterogeneity in the 2.7 Å distances. Figure 2 shows several structures that are consistent with this result. The number of possible structures can be largely reduced, when, in addition, the constraint of one 3.3 Å Mn–Mn distance is taken into account, which stems from fits to Fourier peak III in untreated and Ca-depleted PS II samples.^{11,98} In this case, only structures **A**, **E**, **F**, **G**, and **K** are likely, because the others have either none (**C**, **J**), two (**B**, **D**, **I**), or three (**H**) ~3.3 Å Mn–Mn distances.

From the remaining structures with two di- μ -oxo-bridged Mn–Mn moieties (**A**, **E**, **F**, and **K**), structure **A** was favored for a long time because of its simplicity.¹⁰ However, on the basis of simulations of EPR spectra from the S_2 state, Peloquin et al.³² prefer structures **E** or **F**, because these structures provide better rationale for the strong exchange coupling between two di- μ -oxo Mn–Mn moieties.

Model **G** (Figure 2) is one of the few proposed structures for the OEC that contain three di- μ -oxo type Mn–Mn moieties and one 3.3 Å type Mn–Mn distance.¹¹ This is not surprising because only a few models can be constructed with four Mn ions under these geometrical constraints. However, by moving one of the μ -oxo bridges around, the two new structural models **L** and **M** can be derived (Figure 10). A structure similar to **G** was recently suggested on the basis of simulations of EPR spectra from the S_2 state by Kusunoki and co-workers.^{99,100} In addition, all three structures shown in Figure 10 appear to be consistent with the dimensions of the electron density envelope seen in the 3.8 Å X-ray structure data of the Mn cluster in PS II.^{33,101} However, as confirmed by Mn and Sr EXAFS studies,^{14,15} the OEC is most accurately described as a Mn/Ca heteronuclear cluster; therefore, Ca should be incorporated into each of the proposed structures in Figure 10 so that 1–2 Mn–Ca vectors exist which are oriented close to the membrane normal.¹⁰² It should be noted that Ca has not yet been detected in PS II by X-ray crystallographic studies.

S_0 State

As drawn, the models in Figure 10 are depicted in the S_0 state. On the basis of the detailed discussion in Messinger et al.,³ the Mn oxidation states in the S_0 state are most likely either $\text{Mn}_4(\text{II},\text{III},\text{IV},\text{IV})$ or $\text{Mn}_4(\text{III},\text{III},\text{III},\text{IV})$. The data from the current study are consistent with

both of these options. In Figure 10, only models with three 2.7 Å type Mn–Mn distances and one 3.3 Å vector are shown. As discussed above, models **A**, **E**, **F**, and **K** are also still possibilities, and similar arguments apply to those given below.

In the S_0 state, the presence of Mn(II) and/or protonation of a μ -oxo bridge can account for the increase of one 2.7 Å Mn–Mn distance to 2.85 Å, as explained above. However, in **G**, the presence of Mn(II) in the S_0 state would cause two out of three 2.7 Å Mn–Mn distances to increase, not one out of three. Because this is inconsistent with the EXAFS fits presented in this paper, the use of **G** necessitates assigning the oxidation states of Mn in the S_0 state as $Mn_4(III_3,IV)$ and protonating one of the μ -oxo bridges in the S_0 state (shown in blue in Figure 10).

Each of the remaining two structures in Figure 10, **L** and **M**, can incorporate Mn(II) in the S_0 state and increase only one of the Mn–Mn distances; one possibility is shown in Figure 10. Because it is unclear from model-compound chemistry whether protonation of a μ -oxo bridge would be required, the proton is denoted in blue in Figure 10 as optional for both models; however, protonation of a μ -oxo bridge would most likely be necessary if the $Mn_4(III_3,IV)$ oxidation state option is invoked.

S₃ State

EXAFS experiments on the S_3 state suggest that all of the 2.7 Å Mn–Mn distances in the S_2 state increase in distance in the S_3 state.²⁵ This was explained by Yachandra et al.¹⁶ and Liang et al.²⁵ using **A** in Figure 2 as a structural framework and incorporating an oxyl radical in a μ -oxo bridging position in the S_3 state. This provided an explanation for an increase in distance of one di- μ -oxo-bridged Mn–Mn moiety from 2.7 Å in the S_2 state to 3.0 Å, but it was difficult to understand why, in **A**, the other di- μ -oxo Mn–Mn moiety also increased in distance in the S_3 state even though it was somewhat isolated from the proposed oxyl radical. Thus, it would be more logical if the structure of the OEC was, in fact, more “tied together” than is shown in **A**, which would more easily explain the lengthening of all di- μ -oxo Mn–Mn motifs in the S_3 state.

From the topological models in Figure 10, model **G** seems best suited to understand the structural changes during the S_2 to S_3 transition. If **G** is used, formation of an oxyl radical at the oxygen denoted in red in Figure 10, for example, would give rise to the longer ~3.0 Å Mn–Mn distance in the S_3 state. The lengthening of the other two di- μ -oxo Mn–Mn moieties can be explained if some of the spin density of the oxyl radical in **G** is present on the μ_3 -oxo bridge or the other μ_2 -oxo bridges.

Similarly, one possibility for the di- μ -oxo-bridged oxygen which becomes the oxyl radical and gives rise to the 3.0 Å Mn–Mn distance in the S_3 state is shown in red for structure **L** and **M**. In a fashion similar to what was proposed above for **G**, the increase in the other Mn–Mn distances can be rationalized by some of this spin density being present on the μ_3 -oxo-bridged oxygen and/or the other μ_2 -oxo-bridged oxygens.

Conclusions

The data in this study suggest that three di- μ -oxo Mn–Mn motifs may be present in the OEC. The new topological models shown in Figure 10 evolved from the results presented in this paper and represent new structural possibilities for the OEC that have not been widely considered in previous studies. It is expected that significant insights will come from evaluation of experimental data in terms of these new models. This will be particularly revealing for the interpretations of EXAFS data from oriented PS II membranes in various

S-states^{7,12,81,83} and the interpretation of the ENDOR, ESEEM, and continuous-wave EPR spectra from the S₂ and S₀ states.^{32,103}

Supplementary Material

Refer to Web version on PubMed Central for supplementary material.

Acknowledgments

This research was supported by a National Institutes of Health grant (GM-55302), and the Director, Office of Science, Office of Basic Energy Sciences, Division of Energy Biosciences of the U.S. Department of Energy (DOE), under contract DE-AC03-76SF00098. Synchrotron radiation facilities were provided by the Stanford Synchrotron Radiation Laboratory (SSRL) which is operated by the Department of Energy, Office of Basic Energy Sciences. The SSRL Biotechnology Program is supported by the National Institutes of Health, National Center of Research Resources, Biomedical Technology Program, and by the Department of Energy, Office of Biological and Environmental Research. We thank Wa On Yu for assistance with data collection. J.M. was supported by DFG grants ME 1629/1-1, 2-1, and 2-2. We are indebted to Mel Klein, whose boundless enthusiasm and insightful comments were an inspiration to us throughout this study.

References

1. Kok B, Forbush B, McGloin M. Photochem. Photobiol. 1970; 11:457–475. [PubMed: 5456273]
2. Brudvig GW, Casey JL, Sauer K. Biochim. Biophys. Acta. 1983; 723:366–371.
3. Messinger J, Robblee JH, Bergmann U, Fernandez C, Glatzel P, Visser H, Cinco RM, McFarlane KM, Bellacchio E, Pizarro SA, Cramer SP, Sauer K, Klein MP, Yachandra VK. J. Am. Chem. Soc. 2001; 123:7804–7820. [PubMed: 11493054]
4. Kirby JA, Robertson AS, Smith JP, Thompson AC, Cooper SR, Klein MP. J. Am. Chem. Soc. 1981; 103:5529–5537.
5. Yachandra VK, Guiles RD, McDermott AE, Cole JL, Britt RD, Dexheimer SL, Sauer K, Klein MP. Biochemistry. 1987; 26:5974–5981. [PubMed: 3318924]
6. McDermott AE, Yachandra VK, Guiles RD, Cole JL, Dexheimer SL, Britt RD, Sauer K, Klein MP. Biochemistry. 1988; 27:4021–4031. [PubMed: 2843222]
7. George GN, Prince RC, Cramer SP. Science. 1989; 243:789–791. [PubMed: 2916124]
8. Penner-Hahn JE, Fronko RM, Pecoraro VL, Yocum CF, Betts SD, Bowlby NR. J. Am. Chem. Soc. 1990; 112:2549–2557.
9. MacLachlan DJ, Hallahan BJ, Ruffle SV, Nugent JHA, Evans MCW, Strange RW, Hasnain SS. Biochem. J. 1992; 285:569–576. [PubMed: 1637347]
10. Yachandra VK, DeRose VJ, Latimer MJ, Mukerji I, Sauer K, Klein MP. Science. 1993; 260:675–679. [PubMed: 8480177]
11. DeRose VJ, Mukerji I, Latimer MJ, Yachandra VK, Sauer K, Klein MP. J. Am. Chem. Soc. 1994; 116:5239–5249.
12. Mukerji I, Andrews JC, DeRose VJ, Latimer MJ, Yachandra VK, Sauer K, Klein MP. Biochemistry. 1994; 33:9712–9721. [PubMed: 8068650]
13. Riggs-Gelasco PJ, Mei R, Yocum CF, Penner-Hahn JE. J. Am. Chem. Soc. 1996; 118:2387–2399.
14. Latimer MJ, DeRose VJ, Mukerji I, Yachandra VK, Sauer K, Klein MP. Biochemistry. 1995; 34:10898–10909. [PubMed: 7662671]
15. Cinco RM, Robblee JH, Rompel A, Fernandez C, Yachandra VK, Sauer K, Klein MP. J. Phys. Chem. B. 1998; 102:8248–8256.
16. Yachandra VK, Sauer K, Klein MP. Chem. Rev. 1996; 96:2927–2950. [PubMed: 11848846]
17. Hoganson CW, Babcock GT. Science. 1997; 277:1953–1956. [PubMed: 9302282]
18. Renger G. Physiol. Plant. 1997; 100:828–841.
19. Siegbahn PEM, Crabtree RH. J. Am. Chem. Soc. 1999; 121:117–127.
20. Limburg J, Szalai VA, Brudvig GW. J. Chem. Soc., Dalton Trans. 1999:1353–1362.
21. Messinger J. Biochim. Biophys. Acta. 2000; 1459:481–488. [PubMed: 11004466]

22. Robblee JH, Cinco RM, Yachandra VK. *Biochim. Biophys. Acta*. 2001; 1503:7–23. [PubMed: 11115621]
23. Bertagnolli H, Ertel TS. *Angew. Chem., Int. Ed. Engl.* 1994; 33:45–66.
24. Guiles RD, Yachandra VK, McDermott AE, Cole JL, Dexheimer SL, Britt RD, Sauer K, Klein MP. *Biochemistry*. 1990; 29:486–496. [PubMed: 2154248]
25. Liang W, Roelofs TA, Cinco RM, Rompel A, Latimer MJ, Yu WO, Sauer K, Klein MP, Yachandra VK. *J. Am. Chem. Soc.* 2000; 122:3399–3412.
26. Messinger, J.; Robblee, JH.; Fernandez, C.; Cinco, RM.; Visser, H.; Bergmann, U.; Glatzel, P.; Cramer, SP.; Campbell, KA.; Peloquin, JM.; Britt, RD.; Sauer, K.; Yachandra, VK.; Klein, MP. *Photosyn-thesis: Mechanisms and Effects*. Garab, G., editor. Vol. 2. Kluwer Academic Publishers; Dordrecht: 1998. p. 1279–1282.
27. Dau H, Iuzzolino L, Dittmer J. *Biochim. Biophys. Acta*. 2001; 1503:24–39. [PubMed: 11115622]
28. Messinger J, Robblee J, Yu WO, Sauer K, Yachandra VK, Klein MP. *J. Am. Chem. Soc.* 1997; 119:11349–11350.
29. Sauer, K.; Yachandra, VK.; Britt, RD.; Klein, MP. *Manganese Redox Enzymes*. Pecoraro, VL., editor. VCH Publishers; New York: 1992. p. 141–175.
30. Siegbahn PE. *M. Inorg. Chem.* 2000; 39:2923–2935.
31. Limburg, J.; Brudvig, GW.; Crabtree, RH. *Biomimetic Oxidations Catalyzed by Transition Metal Complexes*. Meunier, B., editor. Imperial College Press; London: 2000. p. 509–541.
32. Peloquin JM, Campbell KA, Randall DW, Evanchik MA, Pecoraro VL, Armstrong WH, Britt RD. *J. Am. Chem. Soc.* 2000; 122:10926–10942.
33. Zouni A, Witt H-T, Kern J, Fromme P, Krauss N, Saenger W, Orth P. *Nature*. 2001; 409:739–743. [PubMed: 11217865]
34. Berthold DA, Babcock GT, Yocum CF. *FEBS Lett.* 1981; 134:231–234.
35. Kuwabara T, Murata N. *Plant Cell Physiol.* 1982; 23:533–539.
36. Porra RJ, Thompson WA, Kriedemann PE. *Biochim. Biophys. Acta*. 1989; 975:384–394.
37. Hanssum B, Dohnt G, Renger G. *Biochim. Biophys. Acta*. 1985; 806:210–220.
38. Babcock GT, Sauer K. *Biochim. Biophys. Acta*. 1973; 325:504–519. [PubMed: 4360258]
39. Styring S, Rutherford AW. *Biochemistry*. 1987; 26:2401–2405.
40. Messinger J, Schröder WP, Renger G. *Biochemistry*. 1993; 32:7658–7668. [PubMed: 8347576]
41. Messinger J, Nugent JHA, Evans MC. W. *Biochemistry*. 1997; 36:11055–11060.
42. Åhrling KA, Peterson S, Styring S. *Biochemistry*. 1997; 36:13148–13152. [PubMed: 9376375]
43. Rehr JJ, Mustre de Leon J, Zabinsky SI, Albers RC. *J. Am. Chem. Soc.* 1991; 113:5135–5140.
44. Rehr JJ, Albers RC, Zabinsky SI. *Phys. Rev. Lett.* 1992; 69:3397–3400. [PubMed: 10046808]
45. Zabinsky SI, Rehr JJ, Aukudinov A, Albers RC, Eller MJ. *Phys. Rev. B: Condens. Matter*. 1995; 52:2995–3009. [PubMed: 9981373]
46. Rehr JJ, Albers RC. *Rev. Mod. Phys.* 2000; 72:621–654.
47. Sayers DE, Lytle FW, Stern EA. *J. Non-Cryst. Solids*. 1972; 8–10:401–407.
48. Lee PA, Pendry JB. *Phys. Rev. B*. 1975; 11:2795–2811.
49. Lee PA, Citrin PH, Eisenberger P, Kincaid BM. *Rev. Mod. Phys.* 1981; 53:769–806.
50. Teo, BK. *EXAFS: Basic Principles and Data Analysis*. Springer-Verlag; Berlin: 1986.
51. Cinco RM, Rompel A, Visser H, Aromí G, Christou G, Sauer K, Klein MP, Yachandra VK. *Inorg. Chem.* 1999; 38:5988–5998. [PubMed: 11671305]
52. O'Day PA, Rehr JJ, Zabinsky SI, Brown GE Jr. *J. Am. Chem. Soc.* 1994; 116:2938–2949.
53. Franzen L-G, Styring S, Étienne A-L, Hansson Ö, Vernotte C. *Photobiochem. Photobiophys.* 1986; 13:15–28.
54. Yamada Y, Tang X-S, Ito S, Sato K. *Biochim. Biophys. Acta*. 1987; 891:129–137.
55. Enami I, Kamino K, Shen J-R, Satoh K, Katoh S. *Biochim. Biophys. Acta*. 1989; 977:33–39.
56. Noren GH, Boerner RJ, Barry BA. *Biochemistry*. 1991; 30:3943–3950. [PubMed: 1850295]

57. Sandusky, PO.; DeRoo, CLS.; Hicks, DB.; Yocum, CF.; Ghanotakis, DF.; Babcock, GT. The Oxygen Evolving Complex of Photosynthesis. Inoue, Y.; Crofts, AR.; Govindjee; Murata, N.; Renger, G.; Satoh, K., editors. Academic Press; Tokyo: 1983. p. 189-199.
58. Ghanotakis DF, Babcock GT, Yocum CF. *Biochim. Biophys. Acta.* 1984; 765:388–398.
59. Bowes JM, Stewart AC, Bendall DS. *Biochim. Biophys. Acta.* 1983; 725:210–219.
60. Ohno T, Satoh K, Katoh S. *Biochim. Biophys. Acta.* 1986; 852:1–8.
61. Cheniae GM, Martin IF. *Plant Physiol.* 1971; 47:568–575. [PubMed: 16657662]
62. Yocum CF, Yerkes CT, Blankenship RE, Sharp RR, Babcock GT. *Proc. Natl. Acad. Sci. U.S.A.* 1981; 78:7507–7511. [PubMed: 16593134]
63. Ke B, Inoue H, Babcock GT, Fang Z-X, Dolan E. *Biochim. Biophys. Acta.* 1982; 682:297–306.
64. Shen J-R, Satoh K, Katoh S. *Biochim. Biophys. Acta.* 1988; 936:386–394.
65. Pauly S, Witt HT. *Biochim. Biophys. Acta.* 1992; 1099:211–218.
66. Debus RJ. *Biochim. Biophys. Acta.* 1992; 1102:269–352. [PubMed: 1390827]
67. Shulman RG, Eisenberger P, Blumberg WE, Stombaugh NA. *Proc. Natl. Acad. Sci. U.S.A.* 1975; 72:4003–4007. [PubMed: 1060082]
68. Shulman RG, Eisenberger P, Kincaid BM. *Annu. Rev. Biophys. Bioeng.* 1978; 7:559–578. [PubMed: 96725]
69. Teo B-K, Shulman RG, Brown GS, Meixner AE. *J. Am. Chem. Soc.* 1979; 101:5624–5631.
70. George GN, Hilton J, Temple C, Prince RC, Rajagopalan KV. *J. Am. Chem. Soc.* 1999; 121:1256–1266.
71. Hwang J, Krebs C, Huynh BH, Edmondson DE, Theil EC, Penner-Hahn JE. *Science.* 2000; 287:122–125. [PubMed: 10615044]
72. Yachandra VK. *Methods Enzymol.* 1995; 246:638–675. [PubMed: 7752941]
73. Riggs-Gelasco PJ, Shu L, Chen S, Burdi D, Huynh BH, Que L Jr, Stubbe J. *J. Am. Chem. Soc.* 1998; 120:849–860.
74. Penner-Hahn JE. *Struct. Bonding (Berlin).* 1998; 90:1–36.
75. Jaron S, Blackburn NJ. *Biochemistry.* 1999; 38:15086–15096. [PubMed: 10563791]
76. Pidcock E, DeBeer S, Obias HV, Hedman B, Hodgson KO, Karlin KD, Solomon EI. *J. Am. Chem. Soc.* 1999; 121:1870–1878.
77. Bunker, GA.; Hasnain, SS.; Sayers, DE. *X-ray Absorption Fine Structure.* Hasnain, SS., editor. E. Horwood; New York: 1991. p. 751-770.
78. Binsted N, Strange RW, Hasnain SS. *Biochemistry.* 1992; 31:12117–12125. [PubMed: 1280998]
79. Styring S, Rutherford AW. *Biochim. Biophys. Acta.* 1988; 933:378–387.
80. Liang W, Latimer MJ, Dau H, Roelofs TA, Yachandra VK, Sauer K, Klein MP. *Biochemistry.* 1994; 33:4923–4932. [PubMed: 8161553]
81. Dau H, Andrews JC, Roelofs TA, Latimer MJ, Liang W, Yachandra VK, Sauer K, Klein MP. *Biochemistry.* 1995; 34:5274–5287. [PubMed: 7711049]
82. DeRose VJ, Latimer MJ, Zimmermann J-L, Mukerji I, Yachandra VK, Sauer K, Klein MP. *Chem. Phys.* 1995; 194:443–459.
83. Cinco, RM.; Fernandez, C.; Messinger, J.; Robblee, JH.; Visser, H.; McFarlane, KL.; Bergmann, U.; Glatzel, P.; Cramer, SP.; Sauer, K.; Klein, MP.; Yachandra, VK. *Photosynthesis: Mechanisms and Effects.* Garab, G., editor. Vol. 2. Kluwer Academic Publishers; Dordrecht: 1998. p. 1273-1278.
84. Sayers DE, Stern EA, Lytle F. *Phys. Rev. Lett.* 1971; 27:1204–1207.
85. Kurreck J, Garbers A, Reifarth F, Andréasson L-E, Parak F, Renger G. *FEBS Lett.* 1996; 381:53–57. [PubMed: 8641439]
86. Pecoraro, VL. *Manganese Redox Enzymes.* Pecoraro, VL., editor. VCH Publishers; New York: 1992. p. 197-231.
87. Pecoraro, VL.; Hsieh, W-Y. *Manganese and Its Role in Biological Processes.* Sigel, A.; Sigel, H., editors. Vol. 37. Marcel Dekker Inc.; New York: 2000. p. 429-504.
88. Baldwin MJ, Stemmler TL, Riggs-Gelasco PJ, Kirk ML, Penner-Hahn JE, Pecoraro VL. *J. Am. Chem. Soc.* 1994; 116:11349–11356.

89. Christou, G.; Vincent, JB. Metal Clusters in Proteins. Que, L., Jr., editor. Vol. 372. American Chemical Society; Washington, DC: 1988. p. 238-255.
90. Pence LE, Caneschi A, Lippard SJ. *Inorg. Chem.* 1996; 35:3069–3072.
91. Darovsky A, Kezerashvili V, Coppens P, Weyhermüller T, Hummel H, Wieghardt K. *Inorg. Chem.* 1996; 35:6916–6917. [PubMed: 11666866]
92. Bashkin JS, Schake AR, Vincent JB, Chang H-R, Li Q, Huffman JC, Christou G, Hendrickson DN. *J. Chem. Soc., Chem. Commun.* 1988:700–702.
93. Hodgson DJ, Schwartz BJ, Sorrell TN. *Inorg. Chem.* 1989; 28:2226–2228.
94. Mabad B, Cassoux P, Tuchagues J-P, Hendrickson DN. *Inorg. Chem.* 1986; 25:1420–1431.
95. Kessissoglou DP, Butler WM, Pecoraro VL. *Inorg. Chem.* 1987; 26:495–503.
96. Yu SB, Wang CP, Day EP, Holm RH. *Inorg. Chem.* 1991; 30:4067–4074.
97. Kitajima N, Singh UP, Amagai H, Osawa M, Morooka Y. *J. Am. Chem. Soc.* 1991; 113:7757–7758.
98. Latimer MJ, DeRose VJ, Yachandra VK, Sauer K, Klein MP. *J. Phys. Chem. B.* 1998; 102:8257–8265.
99. Hasegawa K, Ono T.-a. Inoue Y, Kusunoki M. *Chem. Phys. Lett.* 1999; 300:9–19.
100. Hasegawa K, Ono T.-a. Inoue Y, Kusunoki M. *Bull. Chem. Soc. Jpn.* 1999; 72:1013–1023.
101. Zouni A, Jordan R, Schlodder E, Fromme P, Witt HT. *Biochim. Biophys. Acta.* 2000; 1457:103–105. [PubMed: 10773155]
102. Cinco RM, Robblee JH, Rompel A, Fernandez C, Sauer K, Yachandra VK, Klein MP. *J. Synchrotron Radiat.* 1999; 6:419–420. [PubMed: 15263329]
103. Britt RD, Peloquin JM, Campbell KA. *Annu. Rev. Biophys. Biomol. Struct.* 2000; 29:463–495. [PubMed: 10940256]

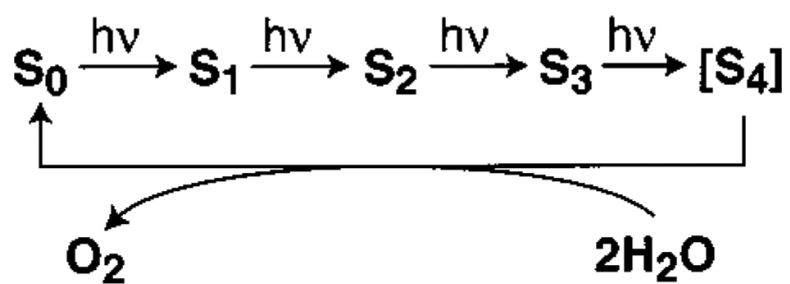


Figure 1.
S-state scheme for oxygen evolution as proposed by Kok et al.¹

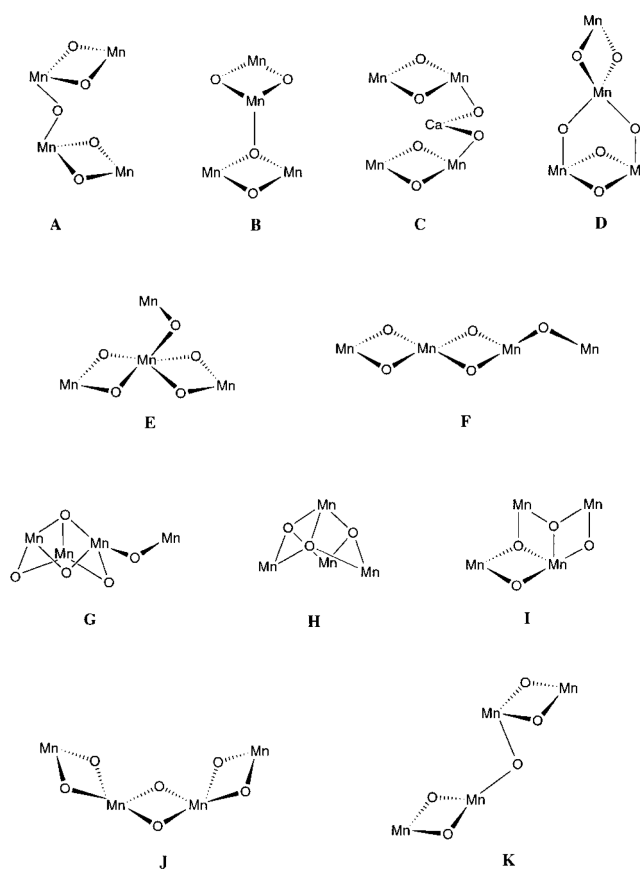


Figure 2.

Possible structural models for the active site of the OEC in PS II. Adapted from DeRose et al.,¹¹ Cinco et al.,⁵¹ and Robblee et al.²²

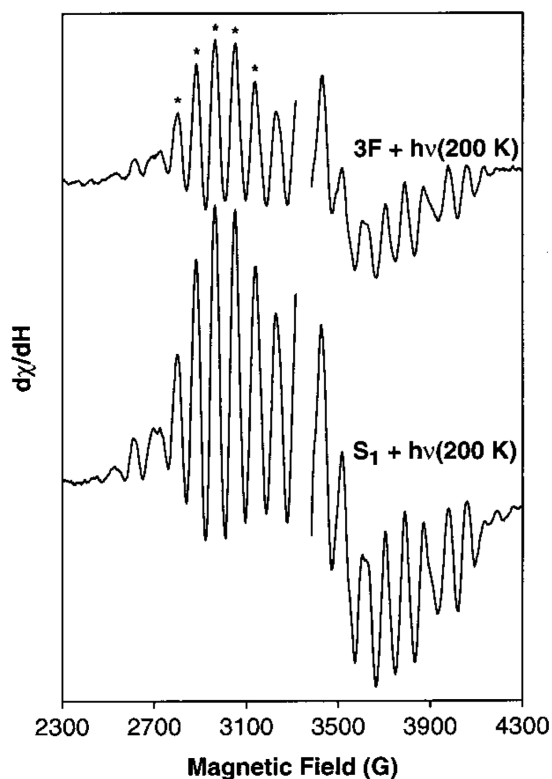


Figure 3.

Use of the S_2 -state multiline EPR signal to quantitate the $S_0:S_1$ ratio in three-flash (3F) samples. A 3F sample and a control S_1 -state sample were continuously illuminated at 200 K for 60 min; the spectra shown above are light-minus-dark difference spectra. The illumination temperature was low enough that only the $S_1 \rightarrow S_2$ transition could proceed; the $S_0 \rightarrow S_1$ and $S_2 \rightarrow S_3$ transitions were cryogenically blocked. The amplitude of the S_2 multiline EPR signal was then measured using the marked peaks. The central region corresponding to Y_D^{ox} has been deleted for clarity. The ratio of the induced S_2 -state multiline EPR signal in the 3F sample relative to that induced in the control S_1 -state sample (50%) corresponds to the percentage of centers in the S_1 state in the three-flash sample before continuous illumination. The addition of FCCP ensures that the only S-states in the 3F sample are the S_0 state and the S_1 state; therefore, the remaining 50% of the centers are poised in the S_0 state. This S-state distribution is used when deconvoluting the EXAFS spectra of the 3F samples.

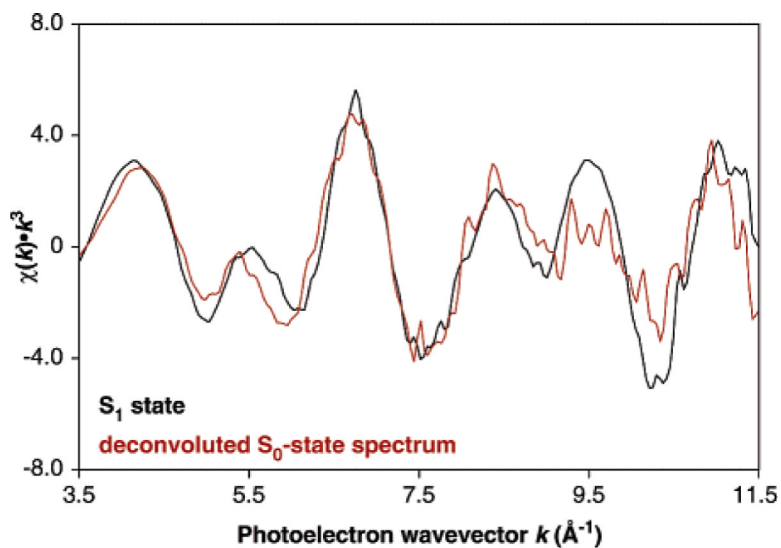


Figure 4.

Average Mn K-edge EXAFS spectra from samples in the S_0 state (red) and samples in the S_1 state (black). The deconvoluted S_0 -state spectrum was calculated from the 3F spectrum and the S_1 -state spectrum using the quantitations from Figure 3 and Table 1 (50% S_0 , 50% S_1). Six 3F samples and six S_1 -state samples (16 scans per sample) were averaged for each spectrum.

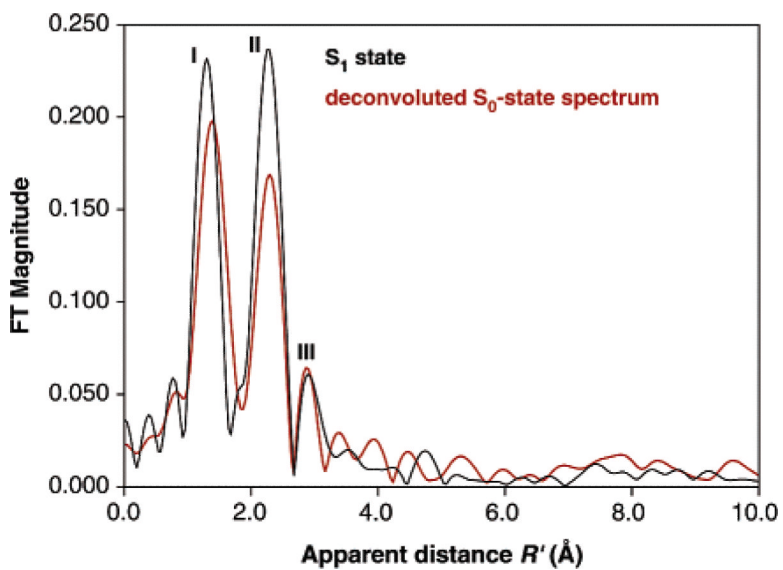


Figure 5. Fourier transforms of the average Mn K-edge EXAFS spectra shown in Figure 4. The Fourier transform corresponding to the S_1 state is shown in black, and the Fourier transform corresponding to the pure S_0 state is shown in red.

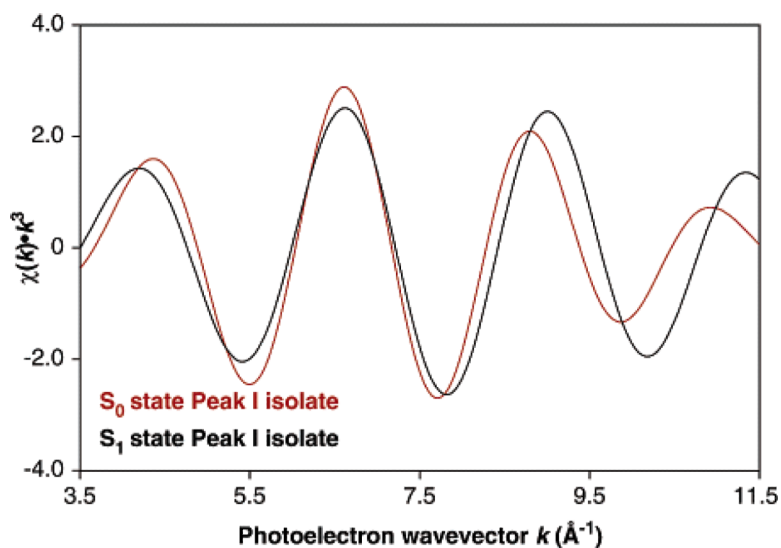


Figure 6.

Fourier isolates from peak I (k^3 -weighted from 3.5 to 11.5 \AA^{-1}) of the Fourier transforms shown in Figure 5. The S_0 state is shown in red, and the S_1 state is shown in black. The difference in the frequency of the EXAFS oscillations between the two S-states is evident. The individual Fourier peaks I, II (Figure 7), and III (Figure 8) were isolated by applying a Hamming window to the first and last 15% of the chosen range, leaving the middle 70% untouched.

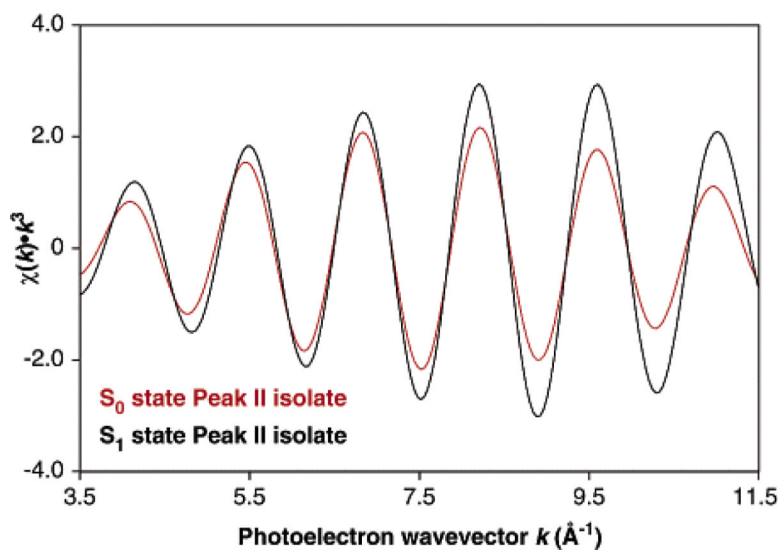


Figure 7.

Fourier isolates from peak II (k^3 -weighted from 3.5 to 11.5 \AA^{-1}) of the Fourier transforms shown in Figure 5. The S_0 state is shown in red, and the S_1 state is shown in black. The difference in the amplitude envelope of the EXAFS oscillations between the two S-states is evident, and can be explained by the presence of two different Mn–Mn distances with a small (<0.2 \AA) separation in distance.

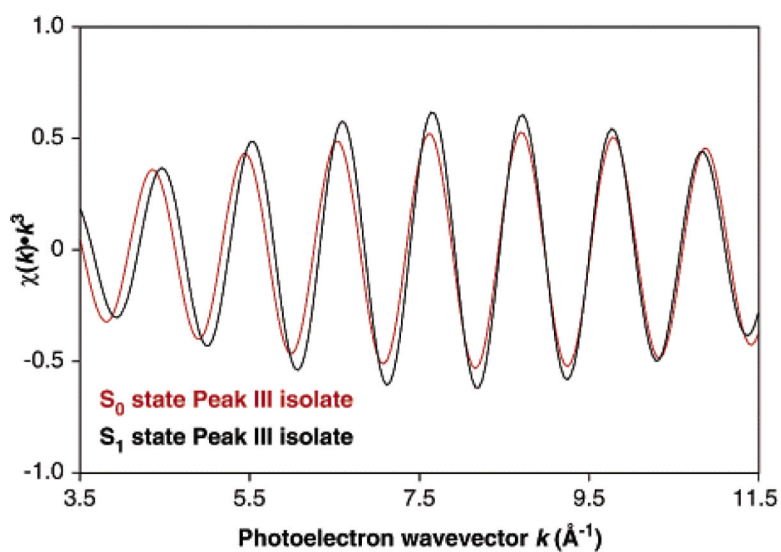


Figure 8. Fourier isolates from peak III (k^3 -weighted from 3.5 to 11.5 \AA^{-1}) of the Fourier transforms shown in Figure 5. The S_0 state is shown in red, and the S_1 state is shown in black.

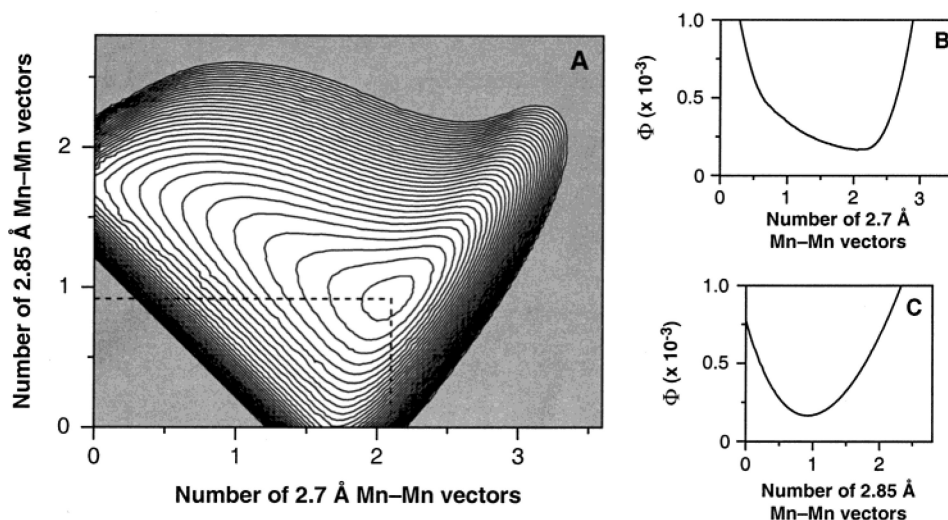
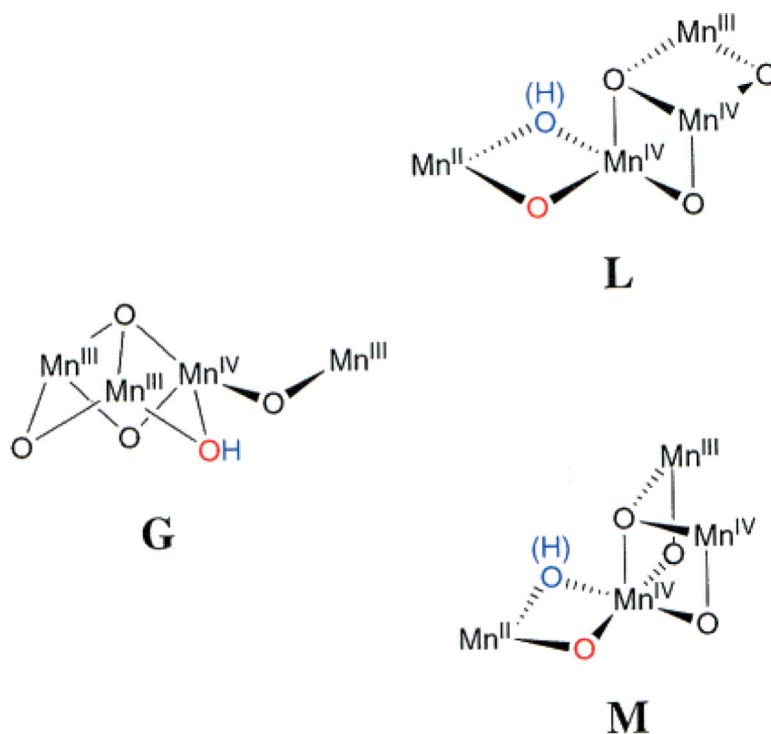


Figure 9.

(A) Contour plot of the Φ error parameter, showing the minimum for the two-shell peak II fit for the S_0 state. For each fit, σ^2 was fixed at 0.002 \AA^2 for each shell, and N_1 and N_2 were fixed at the values corresponding to the designated number of Mn-Mn interactions; according to eq 2, the number of Mn-Mn interactions is twice the N value. The maximum value of Φ shown is 1.0×10^{-3} , and the contour step size is 2.5×10^{-5} error units per contour. The dashed lines designate the fit minimum from fit #17 in Table 3. (B) A vertical section of the contour plot in part A taken at the fixed value of 0.92 Mn-Mn interactions at 2.85 Å (designated by a dashed line in part A). (C) A vertical section of the contour plot in part A taken at the fixed value of 2.1 Mn-Mn interactions at 2.7 Å (designated by a dashed line in part A).

**Figure 10.**

Modified structural models for the active site of the OEC in PS II poised in the S_0 state. Structures **L** and **M** are modifications of **I** or **G** from Figure 2. Each model contains a μ -oxo or a μ -hydroxo bridge colored blue as a suggestion for the Mn–Mn moiety giving rise to the 2.85 Å Mn–Mn distance; the two remaining di- μ -oxo Mn–Mn distances are 2.7 Å. A possible site of the proposed oxyl radical in the S_3 state is denoted in red for each model (see text for details). Mn oxidation states in the S_0 state can be either $Mn_4(III_3,IV)$ or $Mn_4(II,III,IV_2)$.

Table 1

S-State Distribution Results from Measurements of the Light-Induced S₂-State Multiline EPR Signal in Three-Flash Samples and Control S₁-State Samples^a

sample	$(3\text{-flash} + h\nu(200\text{ K})) / (S_1 + h\nu(200\text{ K}))$	S ₀ -state population
S ₀ #1	0.487	51.3%
S ₀ #2	0.498	50.2%

^aThe spectra used in the calculation of the values for sample S₀ #2 are shown in Figure 3.

Table 2

One- and Two-Shell Simulations of Fourier Peak I of the S₀-State Samples (Fit #7 Corresponds to the Average of the Fit Parameters from Fits #1–6, while Fits #8 and #10 Are Fits to the Average S₀-State Spectrum)

fit #	sample	shell	<i>R</i> (Å)	<i>N</i>	σ^2 (Å ²)	ΔE_0 ^b	Φ (×10 ³)	ε^2 (×10 ⁵)
One Shell								
1	S ₀ A	Mn–O	1.86	2.5 ^c	0.005	–20	0.83	0.75
2	S ₀ B	Mn–O	1.85	2.5 ^c	0.005	–20	0.47	0.40
3	S ₀ C	Mn–O	1.87	2.5 ^c	0.003	–19	0.58	0.49
4	S ₀ D	Mn–O	1.87	2.5 ^c	0.006	–19	0.39	0.29
5	S ₀ E	Mn–O	1.88	2.5 ^c	0.004	–15	0.66	0.62
6	S ₀ F	Mn–O	1.85	2.5 ^c	0.004	–20	0.59	0.55
7	average	Mn–O	1.86	2.5 ^c	0.004	–19	0.59	0.52
8	S ₀ grand add	Mn–O	1.86	2.5 ^c	0.005	–19	0.56	0.48
9	S ₁	Mn–O	1.84	2.5 ^c	0.005	–20	1.47	1.61
Two Shells								
10 ^e	S ₀ grand add	Mn–O	1.86	2.5 ^c	0.005	–20	0.37	0.61
		Mn–O	2.24	3.5 ^c	0.025 ^d			
11 ^e	S ₁	Mn–O	1.84	2.5 ^c	0.004	–20	1.13	5.93
		Mn–O	2.05	3.5 ^c	0.025 ^d			

^a Fit parameters and quality-of-fit parameters are described in Materials and Methods.

^b ΔE_0 was constrained to be equal for all shells within a fit.

^c Parameter fixed in fit.

^d Upper limit for parameter.

^e See text for details.

Table 3

One- and Two-Shell Simulations of Fourier Peak II from the S₀-State Samples (Fits #7 and #16 Correspond to the Average of the Fit Parameters from Fits #1–6 and #10–15, Respectively, while Fits #8 and #17 Are Fits to the Average S₀-State Spectrum)

fit #	sample	shell	<i>R</i> (Å)	<i>N</i>	σ^2 (Å ²)	ΔE_0^b	Φ (×10 ³)	ϵ^2 (×10 ⁵)
One Shell								
1	S ₀ A	Mn–Mn	2.71	0.94	0.003	–20	0.66	0.92
2	S ₀ B	Mn–Mn	2.72	1.31	0.005	–20	0.39	0.51
3	S ₀ C	Mn–Mn	2.73	1.38	0.004	–20	0.19	0.28
4	S ₀ D	Mn–Mn	2.74	1.56	0.005	–17	0.24	0.36
5	S ₀ E	Mn–Mn	2.73	1.26	0.005	–18	0.24	0.39
6	S ₀ F	Mn–Mn	2.74	1.38	0.004	–17	0.23	0.41
7	average	Mn–Mn	2.73	1.30	0.004	–19	0.32	0.48
8	S ₀ grand add	Mn–Mn	2.72	1.30	0.005	–20	0.27	0.40
9	S ₁	Mn–Mn	2.72	1.26	0.002	–20	0.58	0.63
Two Shells								
10	S ₀ A	Mn–Mn	2.70	0.98	0.002 ^c	–20	0.36	0.91
		Mn–Mn	2.86	0.35	0.002 ^c			
11	S ₀ B	Mn–Mn	2.71	1.02	0.002 ^c	–18	0.24	0.54
		Mn–Mn	2.85	0.48	0.002 ^c			
12	S ₀ C	Mn–Mn	2.72	1.13	0.002 ^c	–16	0.12	0.35
		Mn–Mn	2.86	0.45	0.002 ^c			
13	S ₀ D	Mn–Mn	2.74	1.17	0.002 ^c	–14	0.14	0.44
		Mn–Mn	2.87	0.56	0.002 ^c			
14	S ₀ E	Mn–Mn	2.73	0.99	0.002 ^c	–14	0.13	0.48
		Mn–Mn	2.87	0.46	0.002 ^c			
15	S ₀ F	Mn–Mn	2.74	1.16	0.002 ^c	–13	0.12	0.65
		Mn–Mn	2.88	0.48	0.002 ^c			
16	average	Mn–Mn	2.72	1.08	0.002 ^c	–16	0.19	0.56
		Mn–Mn	2.86	0.46	0.002 ^c			
17	S ₀ grand add	Mn–Mn	2.72	1.05	0.002 ^c	–16	0.17	0.50
		Mn–Mn	2.86	0.46	0.002 ^c			
18	S ₁	Mn–Mn	2.74	1.51	0.002 ^c	–14	0.47	0.73
		Mn–Mn	2.90	0.55	0.002 ^c			

^a Fit parameters and quality-of-fit parameters are described in Materials and Methods.

^b ΔE_0 was constrained to be equal for all shells within a fit.

^c Parameter fixed in fit.

Table 4

Two-Shell Simulations of Fourier Peak II from the S₀-State Samples in which N_1 and N_2 for the Two Shells Were Fixed in Either a 1:1 or a 2:1 Ratio (Fits #7 and #16 Correspond to the Average of the Fit Parameters from Fits #1–6 and #10–15, Respectively, while Fits #8 and #17 Are Fits to the Average S₀-State Spectrum)

fit #	sample	shell	R (Å)	N	σ^2 (Å ²)	ΔE_0^b	Φ (×10 ³)	ϵ^2 (×10 ⁵)
$N_1:N_2 = 1:1$								
1	S ₀ A	Mn–Mn	2.67	0.48 ^d	0.002 ^c	−20	0.64	0.89
		Mn–Mn	2.75	0.48 ^d	0.002 ^c			
2	S ₀ B	Mn–Mn	2.68	0.66 ^d	0.002 ^c	−20	0.35	0.46
		Mn–Mn	2.78	0.66 ^d	0.002 ^c			
3	S ₀ C	Mn–Mn	2.68	0.69 ^d	0.002 ^c	−19	0.17	0.26
		Mn–Mn	2.78	0.69 ^d	0.002 ^c			
4	S ₀ D	Mn–Mn	2.70	0.77 ^d	0.002 ^c	−17	0.21	0.32
		Mn–Mn	2.80	0.77 ^d	0.002 ^c			
5	S ₀ E	Mn–Mn	2.68	0.62 ^d	0.002 ^c	−18	0.22	0.36
		Mn–Mn	2.79	0.62 ^d	0.002 ^c			
6	S ₀ F	Mn–Mn	2.69	0.68 ^d	0.002 ^c	−17	0.21	0.38
		Mn–Mn	2.79	0.68 ^d	0.002 ^c			
7	average	Mn–Mn	2.68	0.65 ^d	0.002 ^c	−18	0.30	0.44
		Mn–Mn	2.78	0.65 ^d	0.002 ^c			
8	S ₀ grand add	Mn–Mn	2.68	0.65 ^d	0.002 ^c	−20	0.25	0.37
		Mn–Mn	2.77	0.65 ^d	0.002 ^c			
9	S ₁	Mn–Mn	2.70	0.63 ^d	0.002 ^c	−20	0.58	0.63
		Mn–Mn	2.74	0.63 ^d	0.002 ^c			
$N_1:N_2 = 2:1$								
10	S ₀ A	Mn–Mn	2.69	0.97 ^e	0.002 ^c	−20	0.45	0.63
		Mn–Mn	2.83	0.49 ^e	0.002 ^c			
11	S ₀ B	Mn–Mn	2.71	1.02 ^e	0.002 ^c	−18	0.24	0.32
		Mn–Mn	2.85	0.51 ^e	0.002 ^c			
12	S ₀ C	Mn–Mn	2.71	1.03 ^e	0.002 ^c	−17	0.13	0.19
		Mn–Mn	2.83	0.51 ^e	0.002 ^c			
13	S ₀ D	Mn–Mn	2.74	1.16 ^e	0.002 ^c	−14	0.14	0.22
		Mn–Mn	2.87	0.58 ^e	0.002 ^c			
14	S ₀ E	Mn–Mn	2.73	0.98 ^e	0.002 ^c	−14	0.13	0.21

fit #	sample	shell	R (Å)	N	σ^2 (Å ²)	ΔE_0^b	Φ ($\times 10^3$)	ϵ^2 ($\times 10^5$)
15	S ₀ F	Mn–Mn	2.86	0.49 ^e	0.002 ^c	–14	0.14	0.26
		Mn–Mn	2.73	1.10 ^e	0.002 ^c			
16	average	Mn–Mn	2.86	0.55 ^e	0.002 ^c	–16	0.20	0.30
		Mn–Mn	2.72	1.04 ^e	0.002 ^c			
17	S ₀ grand add	Mn–Mn	2.85	0.52 ^e	0.002 ^c	–16	0.17	0.26
		Mn–Mn	2.72	1.02 ^e	0.002 ^c			
18	S ₁	Mn–Mn	2.85	0.51 ^e	0.002 ^c	–19	0.57	0.62
		Mn–Mn	2.70	0.93 ^e	0.002 ^c			
		Mn–Mn	2.77	0.46 ^e	0.002 ^c			

^a Fit parameters and quality-of-fit parameters are described in Materials and Methods.

^b ΔE_0 was constrained to be equal for all shells within a fit.

^c Parameter fixed in fit.

^d The $N_1:N_2$ ratio was fixed to 1:1 for this fit.

^e The $N_1:N_2$ ratio was fixed to 2:1 for this fit.

Table 5One- and Two-Shell Simulations of Fourier Peak III from the S₀-State Samples

fit #	sample	shell	<i>R</i> (Å)	<i>N</i>	σ^2 (Å ²)	ΔE_0^b	Φ (×10 ³)	ϵ^2 (×10 ⁵)
1	S ₀ grand add	Mn–Mn	3.33	0.5 ^c	0.004	–13	0.28	0.76
2	S ₀ grand add	Mn–Ca	3.39	0.5 ^c	0.002	–13	0.32	0.87
3	S ₀ grand add	Mn–Mn	3.35	0.5 ^c	0.002 ^c	–8	0.17	0.46
		Mn–Ca	3.57	0.25 ^c	0.002 ^c			
4	S ₁	Mn–Mn	3.36	0.5 ^c	0.004	–7	0.25	0.36
5	S ₁	Mn–Ca	3.42	0.5 ^c	0.002	–7	0.28	0.40
6	S ₁	Mn–Mn	3.37	0.5 ^c	0.002 ^c	–3	0.08	0.11
		Mn–Ca	3.58	0.25 ^c	0.002 ^c			

^a Fit parameters and quality-of-fit parameters are described in Materials and Methods.^b ΔE_0 was constrained to be equal for all shells within a fit.^c Parameter fixed in fit.

Table 6

Curve-Fitting Results for Fourier Isolates of Peak II from S-States that Exhibit Distance Heterogeneity in the Di- μ -oxo-bridged Mn–Mn Moieties

S-state	ref	R_1 (Å)	R_2 (Å)	N_1	N_2	$N_1:N_2$
S_0^* state	table III from Guiles et al. ²⁴	2.69	2.87	1.0	0.5	2:1
S_2 ($g = 4.1$) state	table 4B from Liang et al. ⁸⁰	2.72	2.85	0.76	0.44	1.73:1
NH_3 -inhibited S_2 state	table 1 from Dau et al. ⁸¹	2.71	2.86	0.75	0.5	1.5:1
F^- -inhibited S_2 state	table 2 from DeRose et al. ⁸²	2.71	2.85	0.8	0.4	2:1
S_3 state	table 1B from Liang et al. ²⁵	2.82	2.95	0.7	0.4	1.75:1
S_0 state	table 3 from current study	2.72	2.86	1.05	0.46	2.28:1
S_0 state	table 4 from current study	2.72	2.85	1.02	0.51	2:1